NASA TECHNICAL MEMORANDUM

NASA TM X-72679

NASA TM X-72679

(NASA-TM-X-72679) DESIGN AND PRELIMINARY TEST RESULTS AT MACH 5 OF AN AXISYMMETRIC SLOTTED SOUND SHIELD (NASA) 64 p HC $4.50 CSCL 14B

N76-22217

Unclas G3/09 26835

DESIGN AND PRELIMINARY TEST RESULTS AT MACH 5 OF AN AXISYMMETRIC SLOTTED SOUND SHIELD

BY IVAN E. BECKWITH, ANDREW J. SROKOWSKI, WILLIAM D. HARVEY, AND P. CALVIN STAINBACK

NATIONAL AERONAUTICS AND SPACE ADMINISTRATION
LANGLEY RESEARCH CENTER, HAMPTON, VIRGINIA 23665

JUNE 1975

1. Report No.	2. Government Accession No.	3. Recipient's Catalog No.
NASA TM X-72679		

4. Title and Subtitle	5. Report Date
Design and Preliminary Test Results at Mach 5 of an Axisymmetric Slotted Sound Shield	June 1975
	6. Performing Organization Code 37.210

7. Author(s)	8. Performing Organization Report No.
Ivan E. Beckwith, Andrew J. Srokowski, William D. Harvey, and P. Calvin Stainback	
	10. Work Unit No. 505-06-41-01

9. Performing Organization Name and Address	11. Contract or Grant No.
NASA Langley Research Center Hampton, VA 23665	
	13. Type of Report and Period Covered Technical Memorandum

12. Sponsoring Agency Name and Address	14. Sponsoring Agency Code
National Aeronautics and Space Administration Washington, DC 20546	

15. Supplementary Notes

Final release of special information not suitable for formal publication.

16. Abstract

Presented are the basic theory and sound attenuation mechanisms, the design procedures, and preliminary experimental results on a small axisymmetric sound shield for supersonic wind tunnels. The shield consists of an array of small diameter rods aligned nearly parallel to the entrance flow with small gaps between the rods for boundary layer suction. The present results showed that at the lowest test Reynolds number (based on rod diameter) of 5.2×10^4, the noise shield reduced the test section noise by about 60 percent (or 8 dB attenuation) but no attenuation was measured for the higher range of test Reynolds numbers from 7.3×10^4 to 1.9×10^5.

These results are below expectations based on data reported elsewhere on a flat sound shield model. The smaller attenuation from the present tests is attributed to insufficient suction at the gaps to prevent feedback of vacuum manifold noise into the shielded test flow and to insufficient suction to prevent transition of the rod boundary layers to turbulent flow at the higher Reynolds numbers.

17. Key Words (Suggested by Author(s)) (STAR category underlined)	18. Distribution Statement
Supersonic Wind Tunnels sound attenuation boundary layer laminarization .09 Research and Support Facilities (Air)	Unclassified Unlimited

19. Security Classif. (of this report)	20. Security Classif. (of this page)	21. No. of Pages	22. Price*
Unclassified	Unclassified	62	$4.25

*Available from { The National Technical Information Service, Springfield, Virginia 22151
STIF/NASA Scientific and Technical Information Facility, P.O. Box 33, College Park, MD 20740

DESIGN AND PRELIMINARY TEST RESULTS AT MACH 5 OF AN AXISYMMETRIC SLOTTED SOUND SHIELD

By Ivan E. Beckwith, Andrew J. Srokowski, William D. Harvey, and P. Calvin Stainback
Langley Research Center

SUMMARY

The high noise levels of 1 to 8 percent of free stream static pressure found in all existing supersonic wind tunnels for Mach numbers greater than about 3 and at high Reynolds numbers are due to sound radiation from the turbulent boundary layers on the nozzle walls. Laminarization of these turbulent boundary layers reduces the sound radiation by at least an order of magnitude; however, practical methods to achieve laminarization at high Reynolds numbers have not yet been developed.

An alternative technique to reduce the high noise levels is by the use of sound radiation shields. Measurements reported elsewhere of sound attenuation in the "shadow zone" of a flat, rodded-wall, sound shield tested at Mach 6 showed that freestream noise levels were reduced by about 45 percent when the rod boundary layers were laminar. Analysis of these data suggested that about 90 percent (or 20 dB attenuation) of the maximum possible attenuation occurred. The present axisymmetric sound shield utilizes the same basic principle of boundary layer suction through gaps between the rods and the same rod diameter as the flat model; however, in

order to reduce the suction mass flow for boundary layer bleed, the ratio of gap width to rod diameter was reduced from 0.16 on the flat model to 0.068 on the present model.

The present test results indicate that for the lowest test unit Reynolds number of 2.5×10^6 per ft. (8.2×10^6 per m), the input noise from the nozzle was reduced by about 60 percent (or 8 dB attenuation) but little or no sound attenuation occurred for Reynolds numbers from about 3.5×10^6 to 9×10^6 per ft. (11.5×10^6 to 29.5×10^6 per m). The decreased performance of the present model compared with the flat model was attributed to boundary layer transition on the rods and insufficient suction mass flow rates caused by the smaller gap widths. Probably the most important factor involved in the reduced performance of the present model is transition of the rod boundary layers, particularly at the higher Reynolds numbers. New data (not included herein) on the flat shield show that the larger value of gap width to rod diameter ratio of 0.16 is required to maintain laminar flow and achieve the large noise attenuation for the higher Reynolds numbers. Appropriate modifications to the present model to increase the gap spacing are underway.

The purpose of this paper is to present the basic theory, the design procedures, and preliminary experimental results for the axisymmetric sound shield with the small gap width to rod diameter ratio of 0.068. The shield was mounted at the exit of a Mach 5 nozzle. The rods at the forward end of the model were 1/4 inch (0.635 cm) in diameter with average gap spacings between the rods of 0.017 inch (.043 cm) for boundary layer suction.

INTRODUCTION

High noise levels in the free stream of supersonic and hypersonic wind tunnels may modify or invalidate certain types of experimental data (refs. 1 to 5). For Mach numbers greater than about 2.5, this noise is caused primarily by sound radiated from the turbulent boundary layer on the nozzle wall (refs. 6 to 8). As test Reynolds numbers are increased into the range of most technological requirements, reduction of the radiated noise by laminarizing the nozzle wall boundary layer becomes increasingly difficult (refs. 7 and 8). Therefore, as an alternative technique, some type of sound shield or other sound attenuation device or mechanism can be used to control and reduce noise levels in supersonic wind tunnels at high Reynolds numbers (ref. 5). Improved simulation of atmospheric flight and basic aeroacoustic noise studies at higher Reynolds numbers then becomes possible.

The purpose of this paper is to present the basic theory, the design procedures, and preliminary experimental results from an investigation of a sound radiation shield or shroud that consists of a cylindrical array of rods aligned with the flow. The inviscid core flow in the wind tunnel open jet test section is completely enclosed by the array of rods. Internal sound generation is minimized by suction through gaps between the rods for the purpose of maintaining laminar boundary layers on the rods to higher Reynolds numbers than is generally possible on a nozzle wall or a solid wall shroud (ref. 1). To minimize transmission of sound from the suction side of the shield back through the gaps into the shielded flow region, the gap suction flow should be maintained at sonic velocity in

the direction normal to the rods. These techniques were developed and used on a conceptual sound shield model (ref. 9) which consisted of a flat array of 1/4-inch (0.635 cm) diameter rods. Data reported in reference 9 suggested that about 90 percent of the maximum possible reduction in free stream noise levels for this type of flat sound shield occurred during tests at Mach 6. Transition of the rod boundary layers occurred at the rear of the 2 foot (0.6 m) long model at a local unit Reynolds number of about 8×10^6 per foot (2.6×10^7 per m) for a gap width to rod diameter ratio of 0.16. Therefore, it was expected that the use of these same techniques with the axisymmetric sound shield should attenuate free stream noise levels by 20 dB or more for unit Reynolds numbers up to 8×10^6 per ft. (2.6×10^7 per m). However, more recent data for the flat model reported in reference 10 showed the large noise attenuation was not obtained when the ratio of gap width to rod diameter was reduced below 0.16.

SYMBOLS

A	cross sectional area
a	velocity of sound
d	rod diameter
G	eq. (4)
H_e	freestream stagnation enthalpy
g	minimum width of gaps between rods (see fig. 2)
M	Mach number
$\dot{m}$	mass flow
N	total number of rods in sound shield

p	pressure
p'	rms of fluctuating pressure
q	velocity vector in the boundary layer or in free stream (see fig. 2)
R	radius of control volume inner boundary (see fig. 2), or radius of shield and nozzle parts (fig. 9)
Re_θ	momentum thickness Reynolds number
R_∞	unit Reynolds number in free stream of nozzle or shield flow, $\left(\frac{\rho q}{\mu}\right)_\infty$
r	radius from shield centerline to inside surface of cylindrical leading edge (see fig. 2)
$\bar{r}$	radius from shield centerline to minimum gap width (see fig. 2)
s	surface distance around rods from stagnation line (measured normal to rod generators)
T	absolute temperature
t	time
$\bar{u}$	vacuum duct velocity
u	"chordwise" velocity parallel to rod surface and normal to rod generators
V	component of velocity (see fig. 2)
$\tilde{V}$	volume
W	width of rods across the flats (see fig. 2)
x	distance along rods from beginning of full gap spacing (fig. 2); or axial distance from nozzle exit (fig. 12)
y	normal distance from surface of rods
α	inward inclination angle of rods with respect to model centerline of symmetry (see fig. 2)

β $\cos^{-1} \frac{W}{d}$

γ ratio of specific heats

δ boundary layer thickness at $q/q_e = 0.995$

δ^* displacement thickness of boundary layer based on chordwise component of velocity, $\int_0^\delta \left[1 - \frac{\rho u}{(\rho u)_e}\right] dy$

ε projected angle between rod centerline and edge of flat (see fig. 2)

θ circumferential angular spacing between rods in array (see fig. 2)

$\bar{\theta}$ meridian angle between rod centerline and gap centerline (see fig. 2(b)), $\theta/2$

μ viscosity coefficient

ρ density

ϕ angular distance around rods from windward stagnation line

Subscripts:

av average

box conditions in vacuum box of wind tunnel (fig. 8)

e edge of rod boundary layers

g at minimum width of gaps between rods or at $\phi = 90^\circ$ for pressure orifices

I isentropic Mach number computed from p/p_o (figs. 15 and 16)

N component of velocity or Mach number normal to rod centerline

P component of velocity or Mach number parallel to rod centerline

r at $\phi = 180^\circ$ or leeward side of rods

s suction

T vacuum tank

t	stagnation conditions downstream of normal shock
sℓ	stagnation line of rods ($\phi = 0$)
V	vacuum exhaust duct
w	wall
o	tunnel stagnation conditions
1	values at forward part of shield model where full gap width starts; designated $x = 0$ in equations (5) - (7)
∞	free stream in nozzle or shield flow
*	sonic value
$(\bar{\ })$	overbar is time mean value; or average value in exhaust duct

THEORY AND DESIGN

Basic Requirements and Mechanisms of Rod Wall Noise Shield

Some of the basic requirements and concepts involved in the noise shielding properties of this model are illustrated in figure 1. Figure 1(a) is a sketch (not to scale) showing a side view of the sound shield and its vacuum manifold mounted at the exit of a supersonic nozzle. Figure 1(b) shows corresponding cross-sectional views (also not to scale) of the shield and manifold at a forward station and at a rear or downstream station.

The sound field radiated by supersonic turbulent boundary layers is highly directional in nature and varies in level from about 1 to 8 percent of free stream static pressure (or from about 130 to 150 dB, with reference to 2×10^{-5} N/m^2, depending on the Mach number and static pressure) and includes a very wide band of frequencies up to 150 KHz or more (refs. 6 to 8). Since

the boundary layer on nozzle walls will generally be turbulent at test section length Reynolds numbers of about 10^7 or greater (see ref. 7) a sound shield must be used to reduce stream noise levels for certain types of tests (see ref. 5) at these higher Reynolds numbers. However, to avoid generation and direct radiation of noise into the shielded region from the shield walls (see fig. 1(a)), the boundary layer on the inside walls of the shield must be maintained laminar in spite of the high Reynolds numbers. Laminarization of the internal wall boundary layer is accomplished by partial removal or suction of the boundary layers on the longitudinal rods through small gaps between the rods as illustrated in figure 1(b). As noted on this figure, the radius of the rod array is smaller at the downstream station than at the forward station to compensate for the outward component of the suction flow through the gaps between the rods. Equations required to calculate the fore and aft radii of the rod array, the gap spacing, and other geometric parameters of the model are presented in the next section of this report.

Tests of a conceptual planar model (ref. 9) showed that transition of the rod boundary layers occurred at the rear of the 2 ft. (0.6 m) long model (the diameter of the rods was 0.25 inch (0.635 cm) and the gap width was 0.04 in. (0.012 cm)) at a unit Reynolds number of about 8×10^6 per foot (2.6×10^7 per m) and that local noise levels in the shielded region then began to increase rapidly as R_∞ was increased further. Analysis of the boundary layer behavior on this model (ref. 9) indicated that the flow on each rod was like that on a swept infinite cylinder and therefore the transition Reynolds number should depend mainly on rod diameter and not on the rod length.

The component of velocity parallel to the rods in the inviscid gap flow and in the immediate lee-side region of the gaps is supersonic; hence large

noise levels would also be present in the vacuum manifold external to the shield (fig. 1). To avoid feedback of this external noise into the shielded region, the component of the suction flow normal to the gaps should be maintained sonic by providing pressures in the vacuum chamber or manifold of approximately (0.528) p_∞ (assuming no pressure recovery from the parallel component of the gap flow). The data reported in reference 9 indicated that free stream noise reflection from the inside walls of the shield (fig. 1(a)) was small and suggested that nearly 90 percent of the maximum possible reduction of radiated sound occurred within the shielded region. Hence, it may be concluded that a rod-wall sound shield utilizing these concepts and completely enclosing the test region should provide about 20 dB reduction of stream noise at maximum test Reynolds numbers determined mainly by the shield length and by the observed (ref. 9) unit Reynolds number for transition of 8×10^6 per foot (2.6×10^7 per m). For example, a 4-foot (1.2 m) long shield would provide 20 dB of noise attenuation at a test Reynolds number of approximately 32×10^6 based on the streamwise length of the test region, provided the rod diameter and gap width are comparable with those of the conceptual model (ref. 9).

Calculation of Geometric Parameters for Sound Shield Model

Figure 2 defines the geometric and flow notation to be used in the following equations. This figure is not a design sketch of the model used in the present investigation and is included here solely for the purpose of illustrating the notation, control volume, and velocity components to be used in the following derivations of general design equations which may be used to design any model of this type. The rods are inclined into the flow

by the angle α to compensate for the mean suction flow velocity, V_{N_∞}, normal to the rods. In this way the free stream velocity vector q_∞ is maintained nearly constant throughout the free stream flow region inside the rod array. The number of rods in the array is given by

$$N = \frac{2\pi}{\theta} \tag{1}$$

where for $W_1 = d$ (see fig. 2(a))

$$\theta = 2 \sin^{-1} \frac{d + g_1}{d + 2r} \tag{2}$$

where for small α, r is taken as the radius to the internal tangent point of the rods at $x = 0$. Equations (1) and (2) would generally be used to select the number of rods N and the values of g_1 for given values of r and d. Once N and θ are fixed, the initial gap width g_1 may be increased by machining flats all the way forward on the rods as indicated in fig. 2(b). The relation between W_1, the initial width across the flats, and the corresponding new value of g_1 is then

$$W_1 = \frac{2 \tan \bar{\theta}}{1 + \tan^2 \bar{\theta}} \left\{ G - \left[\left(\frac{d}{2} \right)^2 (1 + \tan^2 \bar{\theta}) - G^2 \tan^2 \bar{\theta} \right]^{1/2} \right\} \tag{3}$$

where

$$G = r + \frac{d}{2} - \frac{g_1}{2 \sin \bar{\theta}} \tag{4}$$

After these initial geometric parameters are determined, the width $W(x)$ across the parallel flats and the gap width $g(x)$ at x are required. These quantities are obtained from a mass conservation equation for the control

volume whose inside surface is the cone frustrum of radii R_1 and $R(x)$ and where the normal velocity is V_{N_∞} (fig. 2(a)). The entrance and exit surfaces of the control volume are cone frustrums of radii, $\bar{r}_1$, R_1, and $\bar{r}(x)$, $R(x)$, respectively. However, the total cross-sectional areas of the inside portion of the rods that protrude into these entrance and exit cone frustrums are subtracted from the frustrum areas. The entrance and exit velocities of V_{P_∞} are taken constant throughout in accordance with the assumption that each rod is like an infinite swept cylinder at angle of attack α. The outer surface of the control volume is taken as the sum of the minimum gap areas for all rods corrected for the δ^* blockage effect at the gap. The velocity at the minimum gap has the two components V_{P_∞} and V_{N^*} (as illustrated in fig. 2(a)). The latter velocity is normal to the rod centerline at the minimum gap and is assumed to be sonic along the entrance edge of the flat. The rods are assumed to be straight and the angles α and ε are taken as constants. The resulting equation for W may be written as

$$\left(\frac{W}{W_1}\right)^2 = 1-2\left(\frac{x}{\bar{r}_1}\right)^2 \sin^2\alpha - \frac{N}{\pi}\left(\sin^{-1}\frac{W_1}{2\bar{r}_1} - \frac{W_1}{2\bar{r}_1}\sqrt{1-\left(\frac{W_1}{2\bar{r}_1}\right)^2}\right)\left[1-\left(\frac{W}{W_1}\right)^2\right]\cos\alpha$$

$$+\frac{N}{\pi}\left(\frac{d}{2\bar{r}_1}\right)^2\left(\cos^{-1}\frac{W_1}{d} + \frac{W_1}{d}\sqrt{1-\left(\frac{W_1}{d}\right)^2} - \cos^{-1}\frac{W}{d} - \frac{W}{d}\sqrt{1-\left(\frac{W}{d}\right)^2}\right)\cos\alpha$$

$$-\frac{N}{\pi}\frac{x}{\bar{r}_1}\left(\frac{p^*}{p_\infty}\sqrt{\frac{T_\infty}{T_*}}\frac{M_{N^*}}{M_\infty} + \frac{p_*}{p_\infty}\frac{T_\infty}{T_*}\cos\alpha\tan\varepsilon\right)\left[\frac{g_1}{2\bar{r}_1}\left(1+\frac{W}{W_1}\right) - \frac{\delta^*_{1,g}}{\bar{r}_1}\left(1+\frac{\delta^*_g}{\delta^*_{1,g}}\right)\right] \tag{5}$$

where

$$\alpha = \sin^{-1}\left[\frac{\bar{r}_1}{x}\left(1-\frac{W}{W_1}\right) + \frac{d}{2x}\left(\sqrt{1-\left(\frac{W_1}{d}\right)^2} - \sqrt{1-\left(\frac{W}{d}\right)^2}\right)\right] \tag{6}$$

$$\varepsilon = \tan^{-1}\left[\frac{d}{2x}\left(\sqrt{1-\left(\frac{W}{d}\right)^2}-\sqrt{1-\left(\frac{W_1}{d}\right)^2}\right)\right] \tag{7}$$

The relation between $g(x)$ and g_1 has been assumed as

$$\frac{g(x)}{\bar{r}} = \frac{g_1}{\bar{r}_1} \tag{8}$$

where

$$\bar{r} = \frac{W}{2}\,\frac{\left[1+2\frac{g}{W}\cos\bar{\theta}+\left(\frac{g}{W}\right)^2\right]^{1/2}}{\sin\bar{\theta}} \tag{9}$$

This latter equation is also applicable at the initial station. Thus for given values of N, r, d, g_1, x (or length of rods), M_∞, $\delta^*_{1,g}$, and δ^*_g, all geometric parameters of the shield may be computed after solving the above equations for W. Any convenient trial and error procedure may be used for the solution of these equations. Note also that since (α) and (ε) are usually small angles, the above equations may be simplified considerably by utilizing the approximations cos ( ) ≈ 1.0 and sin ( ) ≈ tan( ) ≈ ( ). However, for completeness and accuracy, these approximations were not used in this report.

The pressure and temperature ratios in eq. (5) are computed from the identities

$$\frac{p_*}{p_\infty} \equiv \frac{p_*}{p_{s\ell}}\,\frac{p_{s\ell}}{p_\infty}\,;\quad \frac{T_*}{T_\infty} \equiv \frac{T_*}{T_{s\ell}}\,\frac{T_{s\ell}}{T_\infty} \tag{10}$$

and the assumptions of isentropic cross-flow from the free stream (∞) to the windward stagnation line (sℓ) based on the value of $M_{N,\infty} = M_\infty \sin \alpha$ and isentropic cross-flow from the stagnation line to the minimum gap (*) where sonic cross flow is assumed ($M_{N^*} = 1.0$).

Typical variations of g, W, and α with N for r = 2 in. (5.08 cm) and x = 12.8 in. (32.5 cm) are shown in figure 3 for the case of $W_1 = d$. The variation of g_1, the initial gap, with N is also shown in the figure. The present model has 50 rods, which gives $g_1 = 0.017$ inch (.043 cm), $\alpha = 0.44°$, and W = 0.233 inch (0.592 cm) for $\delta^* = 0$. With finite δ^* (see following section of this report), α and W will be different from these "inviscid" values and they will vary slightly with Reynolds number due to the variation of δ^* with Reynolds number. The rods for the present model (with $W_1 = d$) were machined with W = 0.239 inch (.607 cm) at x = 12.8 in. (32.5 cm) and for the present tests α was set at approximately $0.43°$.

Calculation of Rod Boundary Layer Characteristics

The properties of the boundary layers on the rods were calculated with the swept infinite cylinder program described in reference 11. The inviscid velocity and pressure distributions around the rods (in the "chordwise" direction) are required as inputs for the program. These distributions are based on the variation of the one-dimensional area ratio in the cross flow direction as was done for the flat rod array of reference 9. For all boundary layer calculations presented herein, no viscous corrections (that is no correction for δ^* blockage effects) were applied to this one-dimensional area ratio. However, the calculations for W and α (eqs. (5) - (7)) and the suction mass flow may include the viscous effect through the δ^* factors.

Comparisons with measured pressures (ref. 9) for the flat rod array showed this procedure gave satisfactory estimates of pressure distributions. For the present model, the sonic throat for circular rods with flats is located at $\phi = \pi/2 - \theta/2$ for $W_1 = d$ and at $\phi = \pi/2 - \beta$ for $W_1 < d$ (see fig. 2(b)) rather than at $\phi = \pi/2$ for the model of reference 9. This shift of the sonic throat and the effect of the variation in flats from the front to the rear of the rods were accounted for. The sweep angle also required as an input to the numerical code is $\frac{\pi}{2} - \alpha$ where α is obtained from equation (6).

The variations of δ and δ^* with s around the rods are shown for the present model at typical conditions in figure 4. Since $g_1/d = 0.068$, it can be seen that for this calculation (assuming $\delta^* = 0$ to get the inviscid pressure distribution and using the inviscid α from fig. 3) the flow in the gaps is essentially filled with boundary layer, and "blockage" effects due to the displacement effect of the boundary layer flow would be significant.

Since δ^* varies with unit Reynolds number, α and W from equations (5) and (6) also vary with unit Reynolds number as illustrated in figure 5 for three different values of g_1 for the present model with $N = 50$ rods. Thus, for a given value of g_1, α should be increased appreciably with increasing unit Reynolds number (fig. 5(a)) while W at $x = 12.8$ in. (32.5 cm) is more nearly constant (fig. 5(b)). The present model was therefore designed to provide for adjustable rod inclination by means of screw supports at the rear of the rods. However, the only practical way to change the gap size on the present model is to machine larger flats on the rods.

The variations with unit Reynolds number of boundary layer thickness parameters at the gap, δ_g and δ^*_g, are shown in figure 6. This figure

shows that for $g_1/d = 0.068$ and laminar boundary layers that fully viscous gap flow, or merging of the boundary layers on adjoining rods would occur for $R_\infty < 8.5 \times 10^6$ (27.9×10^6 per m). For the two higher values of g_1/d, fully viscous gap flow would not occur for unit Reynolds numbers above approximately 2×10^6 per ft (6.6×10^6 per m).

As reported in reference 9, transition occurred on the flat array of 1/4-inch (0.635 cm) diameter rods at $R_\infty \simeq 8 \times 10^6$ per ft. (26×10^6 per m) for $M_\infty = 6$ and a gap setting of $g/d = 0.16$. This transition Reynolds number agreed with the freestream Reynolds number based on rod diameter for transition on swept cylinders with spanwise contamination from tip or end disturbances (ref. 12). Another transition parameter that should be considered according to Pfenninger (ref. 13) is the momentum thickness Reynolds number at the stagnation line. The variation of this parameter with R_∞ is shown in figure 7(a) for the present model and test conditions with three values of g_1/d and for the corresponding conditions of reference 9 with $g_1/d = 0.16$. Pfenninger's criteria for transition with and without spanwise contamination on the leading edge of a swept wing (based on data for sweep angles from 30° to 45°) are also shown in the figure. These criteria indicate that transition would occur at the stagnation line of the rods for the present conditions and also the conditions of reference 9 over essentially the entire test range. However, as mentioned previously, transition occurred at $R_\infty/\text{ft} \simeq 8 \times 10^6$ for the previous tests (ref. 9) which would give $Re_{\theta,P,s\ell} = 390$ for transition. If this momentum thickness Reynolds number is assumed to be the appropriate transition criteria for both the present and previous model, then transition would be expected at values of $R_\infty \simeq 4.5 \times 10^6$, 7.7×10^6, and 10.2×10^6 per ft. (14.7×10^6, 25.3×10^6, and 33.5×10^6 per m) for $g_1/d = .068, 0.12$, and 0.16,

respectively, for the present model.

The reason for the difference in the values of $Re_{\theta,P,s\ell}$ for $g_1/d = 0.16$ for the present model and the model of ref. 9 (see fig. 7(a)) is primarily the change in shape of the rods. While the value of d is the same, the present model with $N = 50$ rods has parallel flats on each rod as indicated in Figure 2(b). These flats change the velocity distribution computed by the cross-flow method of reference 9 as shown in Figure 7(b) (for the same cases as fig. 7(a)). The corresponding dimensionless velocity gradient at the stagnation line (listed in fig. 7(b)) is larger for the present model than for the model of reference 9; consequently, the value of $Re_{\theta,P,s\ell}$ at the same R_∞ is reduced.

Final test results, based on measurements of fluctuating pitot pressure in the shielded flow region to determine transition will be used to evaluate the application of the above mentioned and other transition criteria (discussed in ref. 9) for the present sound shield model with $g_1/d = 0.068$ as reported herein and for the other two values of g_1/d when data becomes available.

APPARATUS AND METHODS

Wind Tunnel and Sound Shield

A sketch of the pilot quiet tunnel (ref. 5) which was used to test the sound shield model is shown in figure 8. The slotted Mach 5 nozzle is shown installed in the vacuum box. Measurements of fluctuating flow quantities in this nozzle and in the 11.5-inch (29.2 cm) diameter settling chamber are reported in references 7 and 8. The present test conditions were varied from $p_o \simeq 50$ to 200 lb/in.^{2} (34.5 to 137.9 N/cm^2) corresponding to

$R_\infty \simeq 2.4 \times 10^6$ to 9.5×10^6 per ft. (7.9×10^6 to 31.2×10^6 per m) at $T_o \simeq 640^\circ R$ ($355^\circ K$).

The rod sound shield model is shown mounted at the exit of the slotted nozzle in figure 9. The sharp leading edge(0.006-inch (0.015 cm)thick for the present tests) of the model functions as a scoop to remove the turbulent boundary layer on the nozzle wall and a new laminar boundary layer forms on the inside wall of the shield. By means of a vacuum manifold and ducting system, the pressure on the outside of the rod array, p_v, should be maintained equal to or less than about 1/2 of free stream static pressure inside the shield if no pressure recovery of the parallel component of the flow in the gaps can be obtained. This pressure drop would insure acceleration of the cross-flow normal to the rods to sonic velocity at the minimum gap width.

A photograph of the sound shield model without its vacuum manifold is shown in Figure 10. Pressure orifices were installed on the rods at $\phi = 0^\circ$, 90°, and 180° at distances of 3.5, 8.5, and 13.5 inches (8.9, 21.6, and 34.3 cm) from the leading edge. The inside diameter of the model at the cylindrical sharp leading edge is 4 inches (10.16 cm). The rods are attached to the leading edge cylinder by fairings which start at 1 inch (2.54 cm.) from the leading edge. To compensate approximately for the mean suction flow, the rods are inclined inward at an angle of about 0.4°. (See previous section on "Calculation of Geometric Parameters for Sound Shield Model.) Hence, the inside diameter of the rod array at the rear of the model is approximately 3.82-inches (9.70 cm). Equations for calculating the suction flow requirements will be presented in the next section of this paper.

Suction Mass Flow

Since the pressure in the vacuum manifold may have to be maintained at about 1/2 of stream static pressure, the pipe sizes for the ducting system to the vacuum tank and the volume of the tank must be large enough to avoid excessive viscous losses and short run times. The mass flow through the rod gaps into the vacuum manifold must therefore be calculated as accurately as possible.

For sonic cross-flow at the gaps the suction mass flow is given by the equation

$$\dot{m}_s = \frac{\rho_*}{\rho_\infty} \frac{a_*}{a_\infty} Nx \left(\frac{g_1 + g(x)}{2} - \delta^*_{1,g} - \delta^*_g(x) \right) \rho_\infty a_\infty \qquad (11)$$

where $g(x)$ is computed from equations (8), (9), and (5) and where both g and δ^*_g are assumed to vary linearly with x. Equation (11) is used to determine the vacuum capacity needed and to size the vacuum exhaust pipes to avoid choking and excessive viscous pressure losses. The mean velocity at the entrance to the exhaust pipes is obtained from the general relation

$$\bar{u}_V = \frac{\dot{m}_s}{\rho_V A_V}$$

Then noting that

$$\frac{\rho_*}{\rho_{s\ell}} \frac{a_*}{a_{s\ell}} = \left(\frac{2}{\gamma+1} \right)^{\frac{\gamma+1}{2(\gamma-1)}} = \frac{125}{216} \qquad \text{for } \gamma = 1.4$$

and

$\rho_{s\ell} a_{s\ell} \approx \rho_\infty a_\infty$, we have from Equation (11)

$$\bar{u}_V \approx \frac{125}{216} \frac{T_V/T_o}{p_V/p_\infty} \left(g_{av} - 2\delta^*_{g,av}\right) \frac{a_o}{a_\infty/a_o} \frac{Nx}{A_V} \qquad (12)$$

where $\delta^*_{g,av} = \left(\delta^*_{g,1} + \delta^*_g(x)\right)/2$. The quantities $\bar{u}_V$ and p_V are the mean velocity and pressure at the entrance to the vacuum pipe (or exhaust ducts) as indicated in the following sketch:

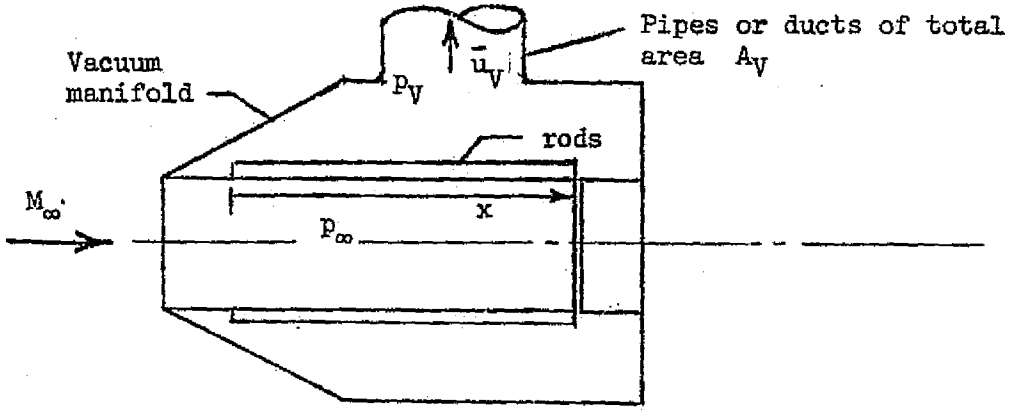

Photographs showing the exhaust duct configuration used during the present tests are presented in figure 11. For the present conditions of $M_\infty \approx 5.0$, and with the requirement that $p_V \leq 0.528\ p_\infty$ Equation (12) becomes

$$\bar{u}_V = 2872 \frac{Nx}{A_V} \left(g_{av} - 2\delta^*_{g,av}\right), \qquad \text{ft/sec.}$$

(875.4) " , m/sec

where $T_V/T_o = 0.85$ and $T_o = 660^oR$. (Experimental values of T_V/T_o varied from 0.862 to 0.875 for the maximum suction mass flows in the present tests.) Obviously, the only way to reduce viscous and other losses in the vacuum ducting system is to reduce $\bar{u}_V$ either by reducing the total slot area formed by the gaps between the rods or by increasing the duct area A_V. For the present model, circumstances required the first choice of reducing the slot area by decreasing the slot width g compared with the values used for the successful tests of reference 9. (Tests on the flat model (ref. 10), completed since the present model was designed and fabricated, have shown that the use of the smaller slot width prevents laminar flow on the rods at the smallest test Reynolds number used herein). Thus with $N = 50$ rods, $g_1 = 0.017$ inch (0.043 cm), $g(x) = 0.016$ inch (0.041 cm), $x = 12.8$ inches (32.5 cm), and $\delta^*_g = 0.005$ inch (.013 cm) corresponding to $R_\infty \approx 9 \times 10^6$ per ft (29.5×10^6 per m) (see fig. 6) we get

$$\bar{u}_V \simeq 152 \text{ ft/sec } (46.4 \text{ m/sec})$$

in the main vacuum pipes to the tank. The area of these pipes is $A_V = 75.5$ in^2 (506.7 cm^2) which corresponds to the two pipes in parallel used for the last series of tests in the present investigation: one 8-inch (20.3 cm) diameter pipe and one 6-inch (15.2 cm) diameter pipe. The vacuum tank used in the present tests has about 3620 ft^3 (85 m^3) of volume which would allow 30 to 40 second long runs depending on the pressure drop through the pipes and the values of δ^*_g.

Test Conditions and Instrumentation

Measurements of mean static pressures, mean pitot pressures, and fluctuating pitot pressures are presented for three different test arrangements as follows:

Test Arrangement	Number and Minimum Diameter of Main Vacuum Pipes			Diffuser Pipe Dia. (see fig. 8)		x location of shield leading edge (see fig. 12)	
		in	cm	in	cm	in	cm
A	one	6	15.2	6.5	16.5	0.125	0.317
B	one	6	15.2	6.5	16.5	-0.250	-0.635
C	two in parallel	6 8	15.2 20.3	8.0	20.3	-0.250	-0.635

When the test series was started, the only vacuum pipe available was a 6-inch (15.2 cm) diameter pipe approximately 175 ft. (53 m) long with eight elbows. Initial results (presented later) using test arrangements A and B indicated that pressure losses were excessive, therefore, a larger pipe was installed in parallel with the first pipe for test arrangement C. The larger pipe consisted of a 10 ft (3 m) length of 8-inch (20.3 cm) diameter pipe followed by a 75 ft (23 m) length of 12-inch (30.5 cm) diameter pipe with four elbows. For test arrangement C, these two pipes were operated in parallel to reduce the viscous losses between the vacuum duct and the tank.

A sketch of the sound shield model and vacuum manifold assembly mounted at the nozzle exit is shown in figure 12. The vacuum manifold is 3 inches (7.6 cm) longer than the sound shield model to increase the efficiency of any pressure recovery from the supersonic streamwise component of the slot

flow. A mean pitot pressure rake with three probes was mounted at the exit of the vacuum manifold as indicated in the figure. These pitot probes were made of steel tubing which was 0.021 inch (0.053 cm) outside diameter and 0.013 inch (0.033 cm.) inside diameter. The probes were spaced 0.25 inch (0.635 cm) apart on the rake. The locations of the fluctuating pitot pressure probe and the corresponding "acoustic origin" points will be described in a later section of this report. For comparative purposes, data obtained in the nozzle without the shield installed will also be shown. These data will be designated as "open nozzle" data. The same fluctuating pitot pressure probes, transducers, and techniques reported in reference 7 were also used in the present investigation.

Static pressure orifices of 0.042-inch (0.107 cm) inside diameter were located on the rods as follows:

Distance from shield leading edge		Stagnation line (s&)	Gap at $\phi = 90^\circ$ (g)	rear or leeward at $\phi = 180^\circ$ (r)
in	cm			
3.5	8.89	✓	✓	
8.5	21.59		✓	✓
13.5	34.29	✓	✓	

A static pressure orifice was also located inside the vacuum manifold on the outside shell near the downstream end of the manifold as shown in figure 12.

RESULTS AND DISCUSSION

Nozzle Wall Static Pressures

To assist in the evaluation of nozzle blockage effects caused by the sound shield and the resulting possible flow disturbances in the vicinity of the shield entrance, four static pressure orifices were installed at 0.25 to 1.00 inch (0.635 to 2.54 cm) upstream of the nozzle exit. These pressure data are shown in figure 13 plotted against the distance from the nozzle exit for several freestream unit Reynolds numbers. The unflagged symbols in figures 13(a), (b), and (c) are for the sound shield installed with test arrangements A, B, and C, respectively, while the flagged symbols in figure 13(b) are data in the open nozzle without the model. Comparison of the data for test arrangements A and B with the open nozzle data show that the sound shield model caused large pressure increases near the nozzle exit, presumably due to the formation and interaction of oblique shocks necessary to increase the nozzle wall pressure to levels approaching those in the tunnel vacuum box. These pressures in the tunnel vacuum box are plotted against R_∞ in figure 14 which shows that the sound shield model always increased the box pressures. Comparison of figures 13(a) and (b) shows the oblique shock strengths were reduced somewhat, at least at the two upstream orifice locations, by moving the model forward into the nozzle. Finally, the oblique shock strengths at all orifice locations were reduced appreciably when the larger diffuser and the larger main vacuum pipes were installed for test arrangement C as shown from the data of fig. 13(c). Thus, the larger diffuser and possibly the increased suction flow rates inside the sound shield model reduced the box pressures

(fig. 14) and relieved the shock interaction problem near the nozzle exit.

Mean Pitot Pressures

Data from the three tube, mean pitot pressure rake mounted at the exit of the vacuum manifold (see fig. 12) and also mounted at the nozzle exit are shown in fig. 15. Comparison of the data at the manifold exit with the open nozzle data show that for test arrangements A and B (figures 15(a) and (b)), flow disturbances were present inside the model. For test arrangement C (fig. 15(c)) disturbances are still present at the two lowest unit Reynolds numbers (by comparison with open nozzle data, fig. 15(b)) but smaller disturbances were present at the two highest unit Reynolds numbers. These results are consistent with those from the nozzle wall static pressure data.

Static Pressures on the Rods and in the Vacuum Manifold

Static pressures measured at $\phi = 0$ on the rods at 3.5 and 13.5 inches (8.89 and 34.29 cm) from the leading edge are shown in figure 16 for the three test arrangements. The pressures at the forward station are nearly the same (with one or two exceptions) as the nozzle wall static pressures for the open nozzle shown in fig. 13(b). Hence, it may be concluded that, in spite of stream disturbances near the center of the model indicated by the pitot pressure data of figure 15, there were no large disturbances near the model wall at this forward station. However, the data at the rear station shows that disturbances were always present there presumably due to local separation caused by the model configuration at its downstream end (note in particular, the sharp leading edge rear support ring in figures 9 and 10) and by the high vacuum box pressures. For test arrangement A, the disturbance at the

rear station was much larger than for test arrangements B and C probably due to stronger shocks or larger disturbances entering the shield from the nozzle as also evidenced by the larger pitot pressures for this test arrangement (fig. 15(a)).

To determine whether sonic cross-flow was present at the gaps between the rods and if any pressure recovery from the supersonic streamwise gap flow occurred within the vacuum manifold, it is convenient to normalize these pressures with the measured rod pressures at $\phi = 0$. Then, if the local inviscid cross-flow at the minimum gaps is sonic, this normalized pressure ratio would be approximately 0.528 (for $\gamma = 1.4$). Since the stagnation line pressure data at the rear station showed the presence of disturbances (see fig. 16) only the $\phi = 0$ data at the forward station (x = 3.5 inches (8.89 cm)) will be used for normalizing purposes. The resulting pressure ratios in the vacuum manifold $(p_v/p_{s\ell})$, at the rear stagnation line of the rods $(p_r/p_{s\ell})$, and at the gaps $(p_g/p_{s\ell})$ are shown in fig. 17. Again, data for the three test arrangements A, B, and C are plotted against R_∞ in figures 17(a), (b), and (c), respectively.

The data in figure 17(a) show that sonic gap flow did not occur for this test arrangement. The suction mass flow reduced the values of $p_r/p_{s\ell}$ to between 0.65 and 0.9 while the gap pressure ratios at the 8.5 inch (21.59 cm) station were above 0.84 except for one point at 0.74. The vacuum manifold pressure is measured at the outside of the manifold at some distance from the rods (fig. 12) where the supersonic gap flow should be mixed and decelerated to lower velocities. On the other hand, the back side rod pressure is measured at $\phi = 180^\circ$ where the cross-flow through the gap is separated and the lowest pressure on the rods should be reached. Therefore, if the ratio of the vacuum manifold pressure to the back side rod pressure, p_v/p_r, is greater than

unity, some pressure recovery has been obtained from the supersonic parallel component of the gap flow. Since the vacuum manifold pressure ratios $p_v/p_{s\ell}$ shown in figure 17(a) are approximately 1.0, some recovery of the supersonic streamwise component of the gap flow was achieved and p_v/p_r varies from about 1.1 to 1.5.

The data for test arrangement B are shown in figure 17(b). The vacuum manifold pressures are reduced somewhat compared with those of test arrangement A, probably because of smaller disturbances inside the model (compare parts (a) and (b) of figs. 15 and 16). The rod pressures were also generally reduced and the pressure recovery in terms of p_v/p_r varied from about 1.1 to 1.3. Again, sonic pressure was not obtained in the gaps.

Figure 17(c) shows the data for test arrangement C which should have considerably more suction mass flow than the other two arrangements due to the larger main vacuum pipes. The vacuum manifold pressures were reduced appreciably at the lower values of R_∞. The rod pressures, both at the gap and at the rear ($\phi = 180^\circ$), were also reduced compared with test arrangement B. However, sonic pressure ratio was not quite attained except at the lowest value of R_∞. Actually, only one data point (for $R_\infty = 2.4 \times 10^6$ per ft (7.9×10^6 per m)) at the gap indicates sonic flow, and since $p_r/p_{s\ell} > 0.528$ for $R_\infty > 4.5 \times 10^6$ per ft (14.8×10^6 per m), it may be concluded that sonic cross-flow was not achieved at the gaps for the three highest test Reynolds numbers. Nevertheless, the pressure recovery was still significant since p_v/p_r varied from about 1.0 to 1.5 as R_∞ was increased over the test range.

The failure to achieve sonic flow for the "best" test arrangement C is believed to be caused by partial choking in the five vacuum exhaust pipes

(see fig. 11) which had the smallest total flow area of the vacuum exhaust system. The choked condition becomes worse at the higher values of R_∞ as evidenced by the increases with increasing R_∞ of $p_V/p_{s\ell}$ and $p_r/p_{s\ell}$ (fig. 17(c)). That is, the suction volume flow increases rapidly with increasing R_∞ due to the decreasing values of δ^*_g as illustrated in figure 6. Thus, if these values of δ^*_g are used in eq. (12) with p_V/p_∞ taken as the measured $p_V/p_{s\ell}$ and with other quantities evaluated according to the discussion immediately following equation (12), the "mean inviscid" velocities at the entrance to the five vacuum exhaust pipes (each of 3 inch (7.62 cm) diameter) are:

$R_\infty \times 10^{-6}$		$\delta^*_{g,av}$		$\bar{u}_V$	
per ft.	per m	in.	cm.	ft/sec.	m/sec.
4.7	15.4	0.0067	0.0170	128	38.7
6.7	22.0	.0056	.0142	177	54
9.0	29.5	.0049	.0124	208	63

For the highest Reynolds number, the value of $\bar{u}_V$ for the main vacuum pipes is about 84 ft/sec (25.7 m/sec) when the measured values of p_V are used. Obviously, the flow area and layout of the exhaust pipes (fig. 11) will have to be improved to relieve the choked condition in these pipes.

Further evidence of choked flow in the vacuum system is apparent from the ratios of the mass flow rate into the vacuum tank to the ideal required mass flow rate through the rod gaps. This latter quantity is obtained from equation (12) and the desired mass flow ratio may then be written as,

$$\frac{\dot{m}_T}{\dot{m}_s} = \frac{\frac{\tilde{V}_T}{T_T}\left(\frac{dp_T}{dt} - \frac{p_T}{T_T}\frac{dT_T}{dt}\right)}{\frac{125}{216}\frac{p_{s\ell}}{p_o}\sqrt{\frac{T_o}{T_{s\ell}}}\left(g_{av} - 2\delta^*_{g,av}\right)\frac{p_o a_o}{T_o}\,Nx} \qquad (13)$$

where $\tilde{V}_T$ is the tank volume, g_{av} is the average gap width, and $\delta^*_{g,av}$ is the average displacement thickness at the gap. At the three highest unit Reynolds numbers for test arrangement C, the values of this ratio (based on measured tank pressures p_T, $p_{s\ell}/p_o$ from figure 16(c), and using $g_{av} = 0.017$* inch (0.043 cm)) are as follows:

$R_\infty \times 10^{-6}$		adjusted $\delta^*_{g,av}$		$\dot{m}_T/\dot{m}_s$
per. ft.	per. m.	in.	cm.	
4.7	15.4	0.0052	0.0132	0.91
6.7	22.0	.0041	.0104	.76
9.0	29.5	.0039	.0099	.74

where the values of $\delta^*_{g,av}$ are based on trends shown in fig. 6 but adjusted slightly (compare with values of $\delta^*_{g,av}$ in the preceeding table) to give more realistic values at the Reynolds numbers where the boundary layer solution for $g_1/d = 0.068$ is not reliable. The above values of $\dot{m}_T/\dot{m}_s$ decrease with increasing tunnel pressure (increasing R_∞) as a result of the increase in the choked flow condition, presumably in the five vacuum

*The actual measured g_{av} was approximately 0.016 inch (.041 cm).

pipes shown in fig. 11. It should be noted that values of p_T and $\frac{dp_T}{dt}$ used in the above calculation were evaluated at 20 seconds after the vacuum valves to the tank were opened. Furthermore, the values of p_V/p_o, $p_{s\ell}/p_o$, and p_g/p_o were essentially invariant with time over at least this elapsed time interval in all runs used herein, and $\frac{dT_T}{dt}$ was assumed negligible.

Schlieren Photographs of Flow at Exit of Sound Shield

To illustrate some of the features of the flow in the sound shield model, figure 18 shows time exposure schlieren photographs of the flow at the exit of the vacuum manifold. Time exposures of 1/5 second were used for these photographs. The flow is from left to right and the small three-tube pitot pressure rake can be seen mounted at the exit. Figures 18(a), (b), and (c) are for test arrangement B at $R_\infty \approx 4.8 \times 10^6$, 7×10^6, and 9.2×10^6 per ft (15.7×10^6, 23.0×10^6, and 30.2×10^6 per m), respectively. Comparison of these three figures indicates that for the two highest Reynolds numbers, the flow in the lower part of the pictures is not as fully started (evidenced by the absence of a shock indicating unsteady flow) as in the upper part where the exit shock appears steady and is therefore clearly evident in these time exposures. This result is consistent with the rod pressure data of figure 17(b) which shows higher pressure ratios at the two highest Reynolds numbers than at the lowest Reynolds number due to less effective suction flow for the former conditions. This effect is again evident by comparing figure 18(b) with figure 18(d) which is at the same unit Reynolds number but for test arrangement C. Thus, the exit shocks are seen clearly in both the upper and lower portions of figure 18(d) due to

both the improved suction flow and the larger tunnel diffuser pipe (see table on page 21). The streaked pattern evident in figures 18(a) - 18(d) is believed to be caused by vortices which have been observed on the flat model (reference 9) under full suction conditions. Thus, when the vacuum exhaust valves are closed, the suction flow through the gaps is cut-off, and the streaked pattern has practically disappeared as shown in figure 18(e).

Measurements of Disturbance Levels With and Without the Sound Shield

Before presentation of the fluctuating pressure measurements in the free stream flow of the nozzle and sound shield, it is necessary to indicate how the pitot probe measurements (the same probes and techniques are used herein as described in reference 7) at a point in the flow are related to upstream sound sources on the nozzle wall. The various stations in the flow where fluctuating pitot pressure data were obtained are shown schematically in figure 12. Each individual station is assigned a number from 1 to 4. The so-called "acoustic origin" (ref. 7) at the nozzle wall or along the rods corresponding to each probe station can be located by tracing a path upstream along the Mach line (from flow field solutions by the method of characteristics for the nozzle flow) from the probe to the wall. The resulting wall points for each probe location are identified with the corresponding probe number. When a probe is off the centerline, such as the number 2 station, the acoustic origins for that probe are located along a skewed curve connecting the number 2 points at the upper and lower wall contours.

The rms pitot pressure data normalized with the mean pitot pressure

at the same point are plotted in Figure 19(a) against the unit Reynolds number in the free stream. The data for stations 1, 2, and 3 are labeled as "no shield" data since the pressures at these points (see fig. 12) can only be influenced by flow conditions in the nozzle and only by disturbances along the nozzle wall at or upstream of the corresponding designated wall points. For a given station, the increase in $p_t'/\bar{p}_t$ starting at low Reynolds numbers is caused by increasing noise when the nozzle boundary layer is still laminar. At somewhat higher Reynolds numbers, the noise levels continue to increase and reach a peak; this behavior is associated with transition from laminar to turbulent flow in the wall boundary layer near or slightly upstream of the corresponding acoustic origin on the wall (refs. 7 and 8). As the tunnel stagnation pressure is increased, the instantaneous time history of the fluctuating pitot pressure obtained at a given point in the flow shows evidence of turbulent bursts which mark the beginning of transition. Thus, the original data for stations 1, 2, and 3 show that transition first occurs at the wall point 3 (4.1 inches (10.4 cm) upstream of the nozzle exit) at $R_\infty \simeq 1.7 \times 10^6$ per ft (5.6×10^6 per m). As R_∞ is increased, transition moves forward to the upper wall point 2 at $R_\infty \simeq 2.7 \times 10^6$ per ft (8.9×10^6 per m) and transition finally occurs at wall point 1 at $R_\infty \simeq 4 \times 10^6$ per ft. (13.1×10^6 per m). These data then represent the noise inputs to the shield flowfield.

Data obtained at station 4 with the sound shield in place (see fig. 12 for the probe location and the corresponding acoustic origin locations on the rods) show no reduction in rms noise compared with data at station 1 in the open nozzle (fig. 19(a)). Compared with open nozzle data at station 3, the shield data at the lowest unit Reynolds number of 2.5×10^6 per ft

(8.2×10^6 per m) for test arrangement C shows that the rms input noise was reduced by about 60 percent (or about 8 dB attenuation). This noise reduction is shown directly in figure 19(b) where the ratio is plotted against R_∞ of data at probe location 4 (test arrangement C) to data at probe location 3 (based on the faired curves in fig. 19(a)). On the basis of these faired curves and the one data point at $R_\infty \approx 2.5 \times 10^6$ per ft (8.2×10^6 per m), it may be concluded that about 60 percent reduction in noise occurred over some small range of R_∞. The large increase in noise for $R_\infty > 4 \times 10^6$ per ft (13.1×10^6 per m) is probably caused by transition on the rods. More data will be required to substantiate these results.

The 60 percent reduction in the input noise is not as much as would be expected from the results reported in reference 9 which suggested that about 90 per cent(or 20 dB) of the maximum possible reduction occurred. The reduced sound attenuation in the present tests of the shield model is probably caused partly by the failure to obtain fully sonic flow in the gaps even for test arrangement C (see figure 17(c)). Another important factor has been revealed by new tests (ref. 10) on the flat model of reference 9 with a gap setting of $g_1/d = 0.068$. Transition of the rod boundary layers occurred at the much lower Reynolds number of about 2×10^6 per ft. (6.6×10^6 per m) rather than the previous value of 8×10^6 per ft (26.2×10^6 per m) observed (ref. 9) with a gap setting of $g_1/d = 0.16$. Hence, transition in the present tests might be expected at this smaller unit Reynolds number. However, according to the present discussion of figure 7, based on the $Re_{\theta,P,s\ell}$ criterion, transition might occur at the higher unit Reynolds number of about

4.5×10^6 per ft (14.8×10^6 per m).* Further tests of the present model with full sonic velocity at the gaps will be conducted to resolve this possible discrepancy. The model is being modified to provide gap spacings of $g_1/d = 0.12$ and 0.16, since reduced noise levels at the higher Reynolds numbers are required for the final desired sound shield (see ref. 5).

CONCLUDING REMARKS

The sound attenuation mechanisms, the design equations, and preliminary test results at Mach 5 of an axisymmetric sound shield are presented. The shield consists of a cylindrical array of 1/4-inch (0.635 cm) diameter rods aligned nearly parallel to the flow. The boundary layer on the rods is partially removed by suction through small gaps between the rods. The gap to rod diameter ratio used in the present tests was 0.068. The purposes of the suction are to delay transition of the rod boundary layers to prevent direct sound radiation into the shielded test region of the flow, and to prevent transmission of vacuum manifold noise into the test region. The cross flow at the minimum gaps between the rods should be sonic.

The present test results indicate that sonic gap flow was not obtained and that no sound attenuation occurred for test Reynolds numbers above

---

*The test data reported in reference 10 have been analyzed in detail and new results regarding trends and parameters of transition, details of the gap flow profiles, and possible pressure recovery for larger gap settings will be presented in an NASA publication by P. C. Stainback, W. D. Harvey, and A. J. Srokowski.

3.5×10^6 per ft (11.5×10^6 per m). At a lower test Reynolds number of 2.5×10^6 per ft (8.2×10^6 per m) the input normalized fluctuating pitot pressure levels were reduced by about 60 percent or roughly by 8 dB.

Data reported elsewhere on a conceptual flat sound shield utilizing the same basic principles and rod diameter as the present model but with a larger gap to diameter ratio of 0.16 showed that free stream noise levels were reduced by about 45 percent. This large noise reduction was achieved only when the rod boundary layers were laminar up to a unit Reynolds number of 8×10^6 per ft (2.6×10^7 per m) and with full sonic cross-flow at the gaps. Analysis of these data suggested that nearly 90 percent (or 20 dB) of the maximum possible noise attenuation occurred under these conditions.

More recent tests on the flat model (not reported herein) with a smaller gap to rod diameter ratio of 0.068 showed much poorer performance caused by the failure to maintain laminar rod boundary layers for Reynolds numbers above 2×10^6 per ft (6.6×10^6 per m). However, at test conditions below this Reynolds number, the large sound attenuation was again obtained.

Hence, it is concluded that the reduced noise attenuation at the lowest Reynolds numbers of the present tests on the axisymmetric shield compared with previous results on the flat model were caused by the failure to achieve full sonic cross-flow at the gaps of the present model. While transition of the rod boundary layers was not measured in the present tests, it is speculated that for the present small gap width, the transition Reynolds number is in the range from 2×10^6 to 4×10^6 per ft (6.6×10^6 to 13×10^6 per m) based on the new results for the flat model and on an analysis included herein of momentum thickness Reynolds number at the stagnation line of the rods. Further tests to verify these predictions are required.

REFERENCES

1. Pate, S. R.; and Schueler, C. J.: Radiated Aerodynamic Noise Effects on Boundary Layer Transition in Supersonic and Hypersonic Wind Tunnels. AIAA Journal, Vol. 7, No. 3, March 1969 , pp 450-457.

2. Stainback, P. C.; Fischer, M. C.; and Wagner, R. D.: Effects of Wind Tunnel Disturbances on Hypersonic Boundary Layer Transition. AIAA Paper No. 72-181, January 1972.

3. Heller, H. H.; and Clemente, A. R.: Unsteady Aerodynamic Loads on Slender Cones at Free-Stream Mach numbers from 0 to 22. AIAA Paper No. 73-998, October 1973.

4. Dods, J. B., Jr.; and Hanly, R. D.: Evaluation of Transonic and Supersonic Wind Tunnel Background Noise and Effects of Surface Pressure Fluctuation Measurements. AIAA Paper No. 72-1004, September 1972.

5. Beckwith, I. E.: Development of a High Reynolds Number Quiet Tunnel for Transition Research. AIAA Paper No. 74-135, January 1974. Also in AIAA Jour., Vol. 13, No. 3, March 1975, pp. 300-306.

6. Laufer, J.: Aerodynamic Noise in Supersonic Wind Tunnels. Journal Aero. Sci., Vol. 28, No. 9, September 1961, pp. 685-692.

7. Stainback, P. C.; Anders, J. B.; Harvey, W. D.; Cary, A. M., Jr.; and Harris, J. E.: An Investigation of Boundary Layer Transition on the Wall of a Mach 5 Nozzle. AIAA Paper No. 74-136, January 1974.

8. Harvey, W. D.; Stainback, P. C.; Anders, J. B.; and Cary, A. M.: Nozzle Wall Boundary-Layer Transition and Freestream Disturbances at Mach 5. AIAA Jour., Vol. 13, No. 3, March 1975, pp. 307-314.

9. Harvey, W. D.; Berger, M. H.; and Stainback, P. C.: Experimental and Theoretical Investigation of a Slotted Noise Shield Model for Wind Tunnel Walls. AIAA Paper No. 74-624, July 1974.

10. Harvey, William D.: Effect of Rod Gap Spacing on a Suction Panel For Laminar Flow and Noise Control in Supersonic Wind Tunnels. M. S. Thesis, Old Dominion University, Norfolk, Virginia, May 1975.

11. Hixon, B. A.; Beckwith, I. E.; and Bushnell, D. M.: Computer Program for Compressible Laminar or Turbulent Nonsimilar Boundary Layers. NASA TM X-2140, April 1971.

12. Bushnell, D. M.; and Huffman, J. K.: Investigation of Heat Transfer to Leading Edge of a 76° Swept Fin With and Without Chordwise Slots and Correlations of Swept-Leading-Edge Transition Data for Mach 2 to 8. NASA TM X-1475, 1967.

13. Pfenninger, Werner; and Reed, Verlin D.: Laminar-Flow Research and Experiments. Astronautics and Aeronautics, Vol. 4, No. 7, July 1966, pp. 44-50.

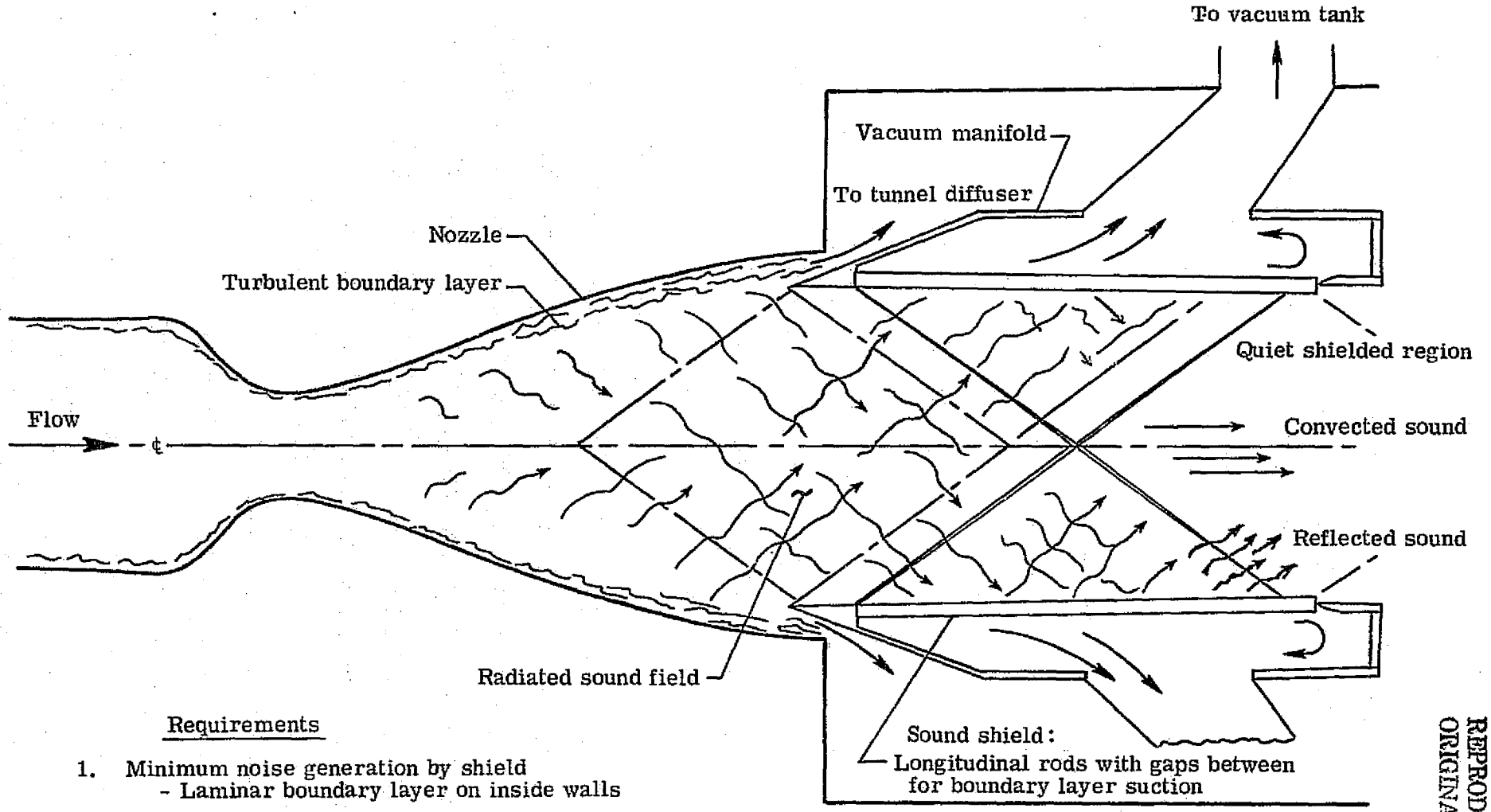

Requirements

1. Minimum noise generation by shield
   - Laminar boundary layer on inside walls
2. Minimum noise reflection
   - Ribbed or anechoic inside walls
   - Sonic gap flow
3. Minimum noise transmission through walls
4. Fabrication tolerances
   - Uniform gaps
   - Straight rods
   - Adjustment requirements

(a) Side view of section through nozzle and shield.

Figure 1.- Concepts and requirements for rodded wall sound shield.

Note : Shape of rod array cross-section could be square or rectangular.
Circular shape illustrated here was used for present model.

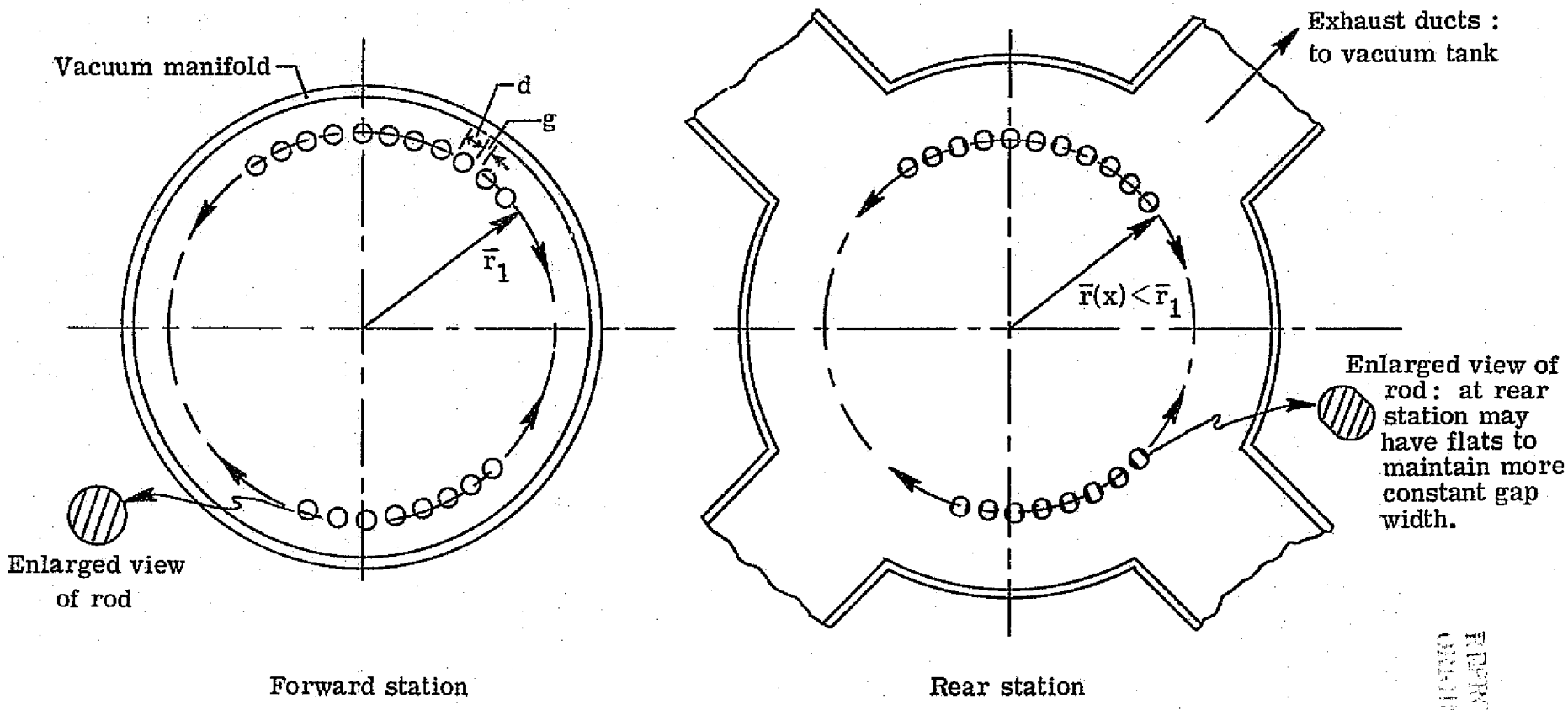

(b) Normal cross-sections through sound shield at two stations.

Figure 1.- Concluded.

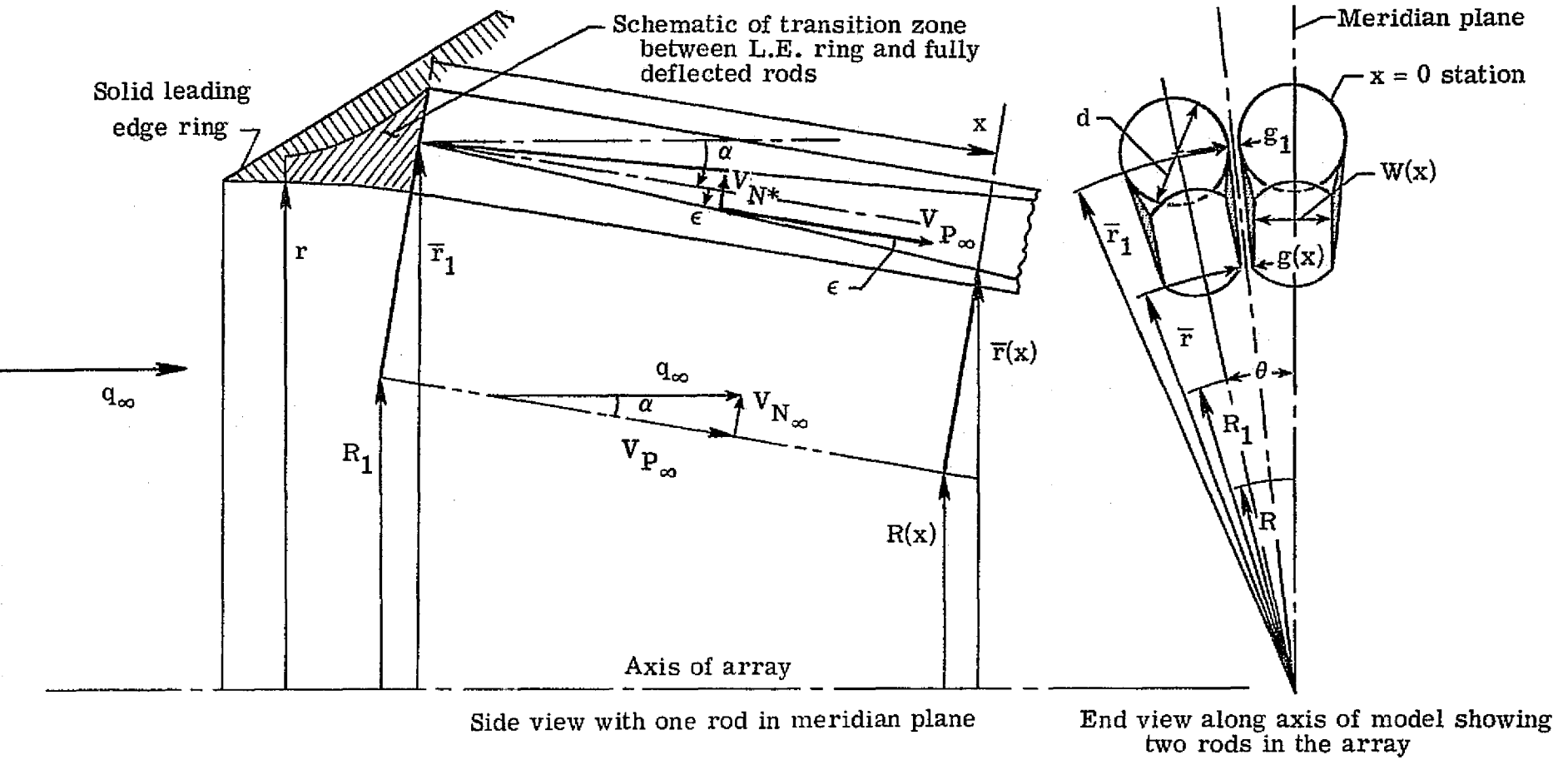

(a) W_1 = d. Rod configuration like that of present model; results are presented herein.

Figure 2.- Definition sketch for control volume of axisymmetric rod array.

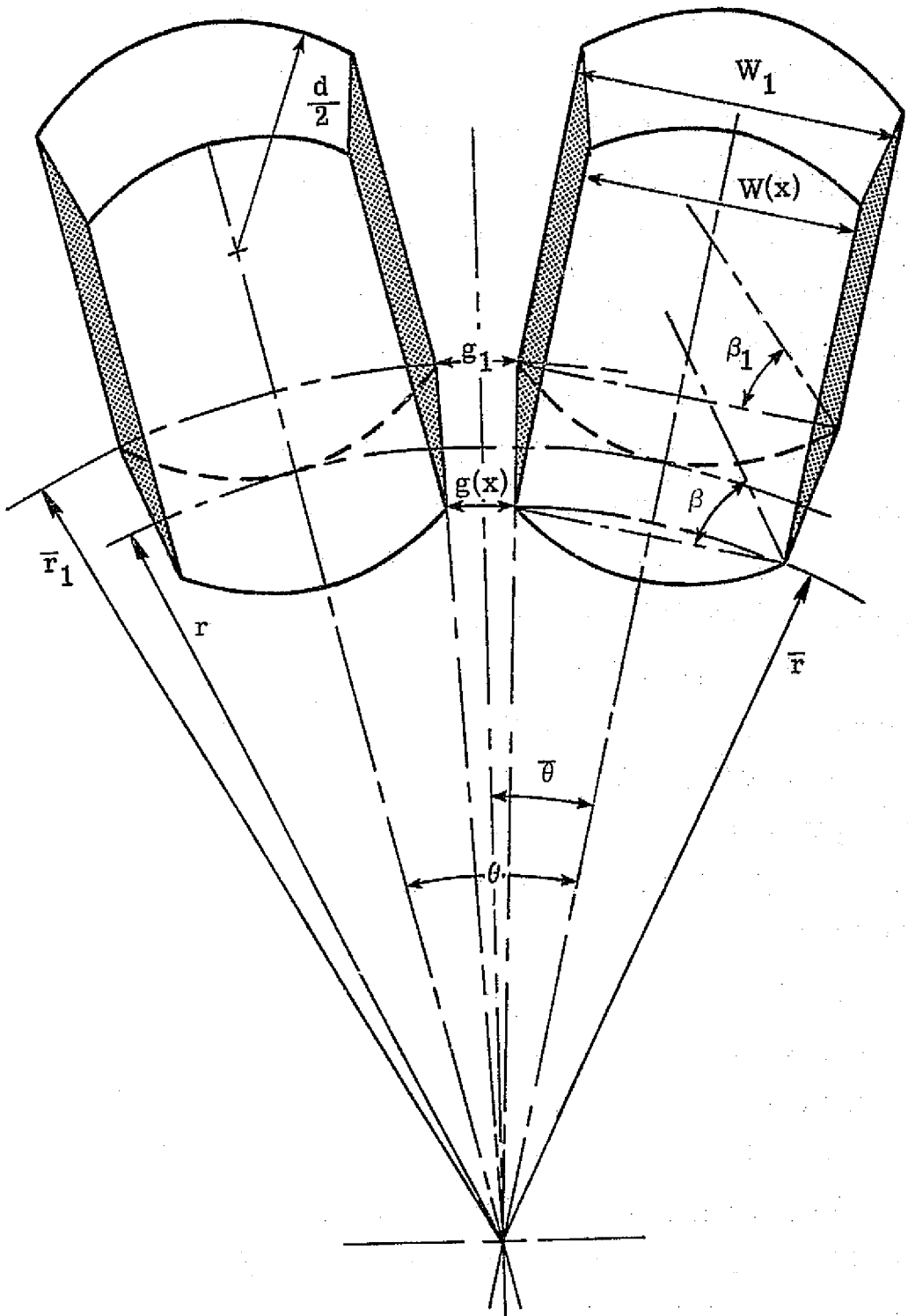

(b) $W_1 < d$. Rod configuration like that of modified model; results not reported herein.

Figure 2.- Concluded.

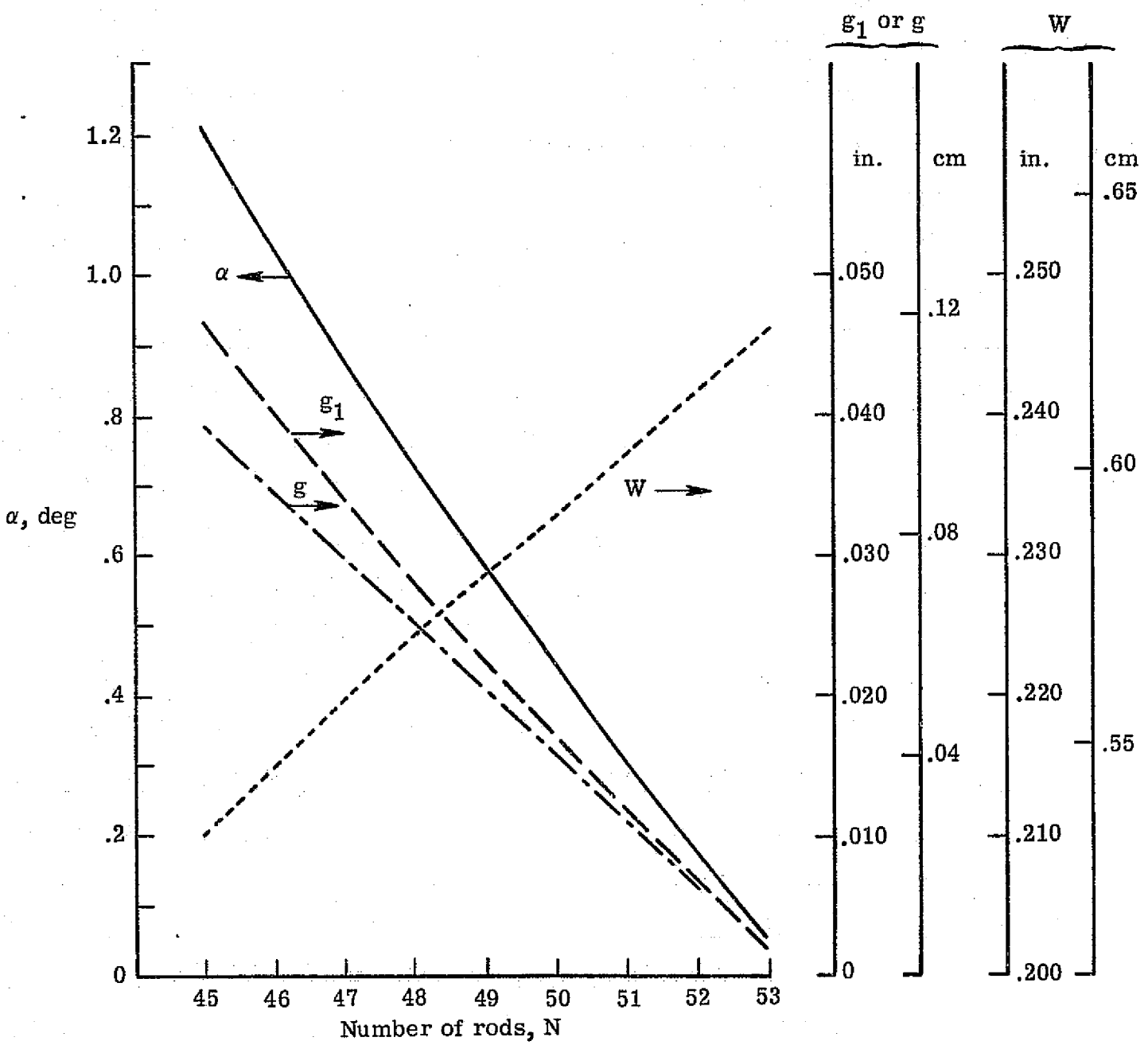

Figure 3.- Variation of geometric parameters of a typical axisymmetric sound shield with N. Values used were r = 2 in.(5.08 cm), x = 12.8 in. (32.5 cm), $\delta^* = 0$, W_1 = d = 0.25 in. (0.635 cm).

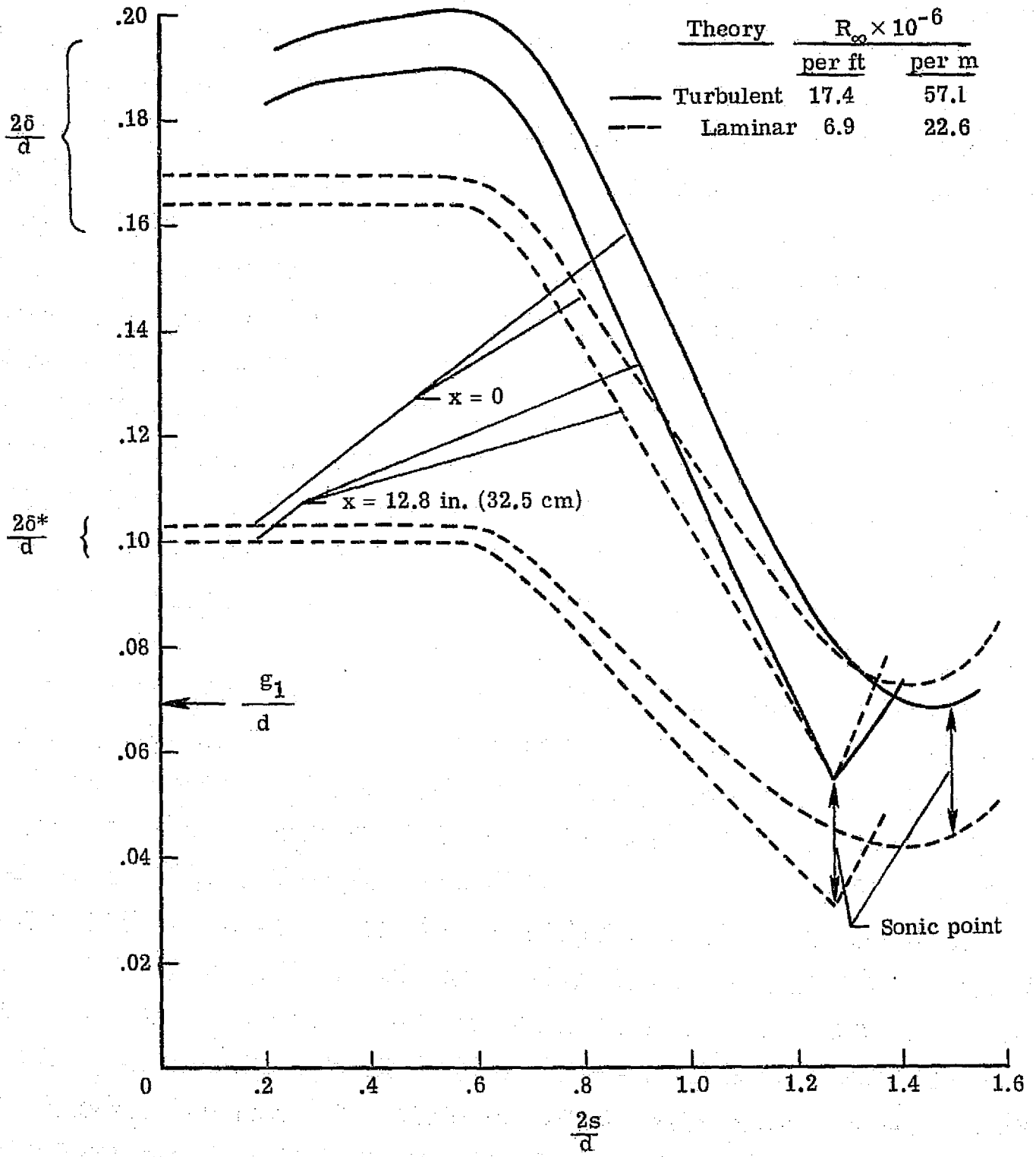

Figure 4.- Boundary layer thickness and displacement thickness variation with distance around rods for typical conditions. W_1 = d, g_1/d = 0.068, d = 0.25 in. (0.635 cm), W = 0.234 in. (0.594 cm) at x = 12.8 in. (32.5 cm).

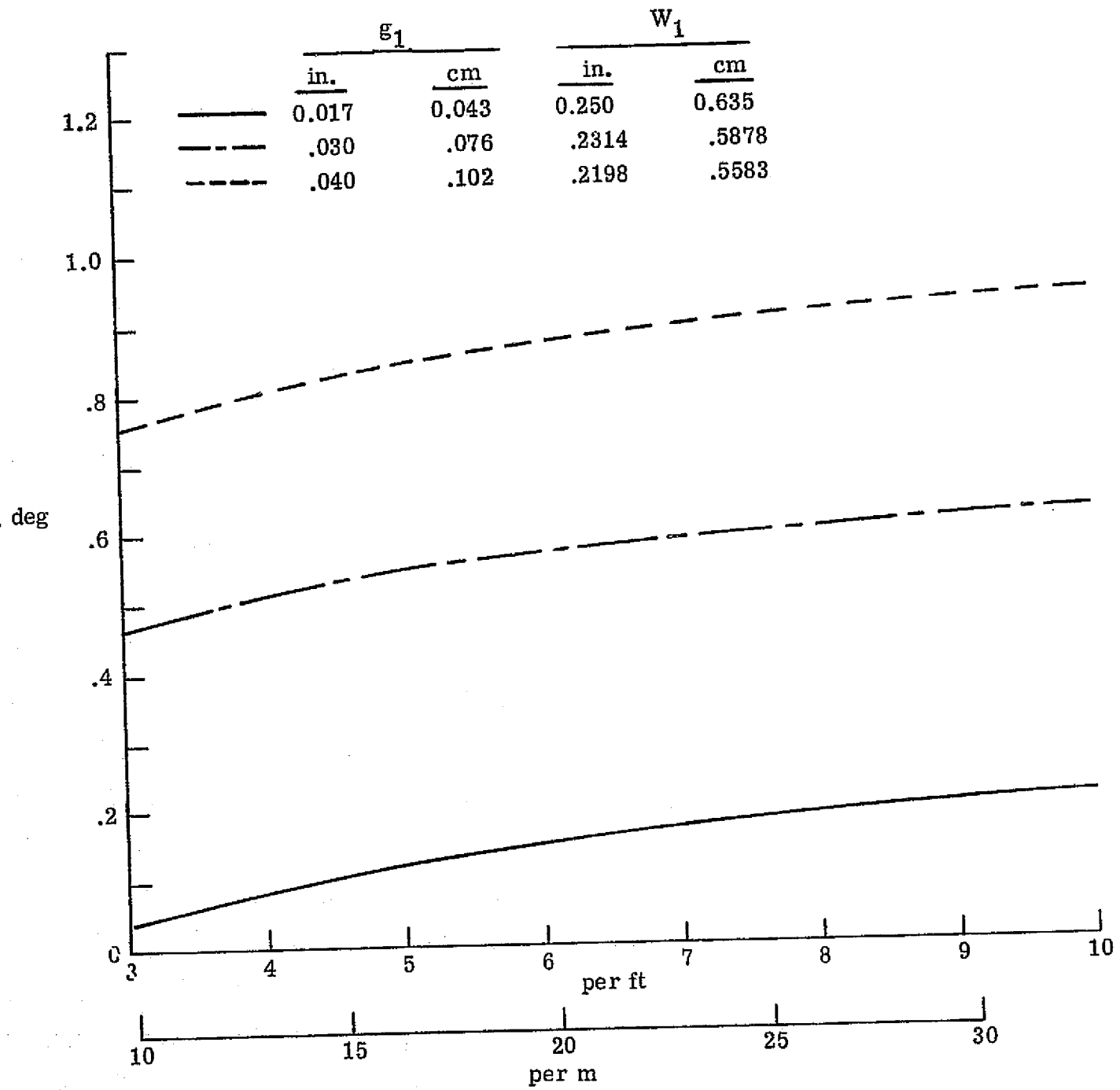

(a) α Variation.

Figure 5.- Variation of geometric parameters with unit Reynolds number for N = 50 rods, d = 0.25 in. (0.635 cm), and r = 2 in. (5.08 cm).

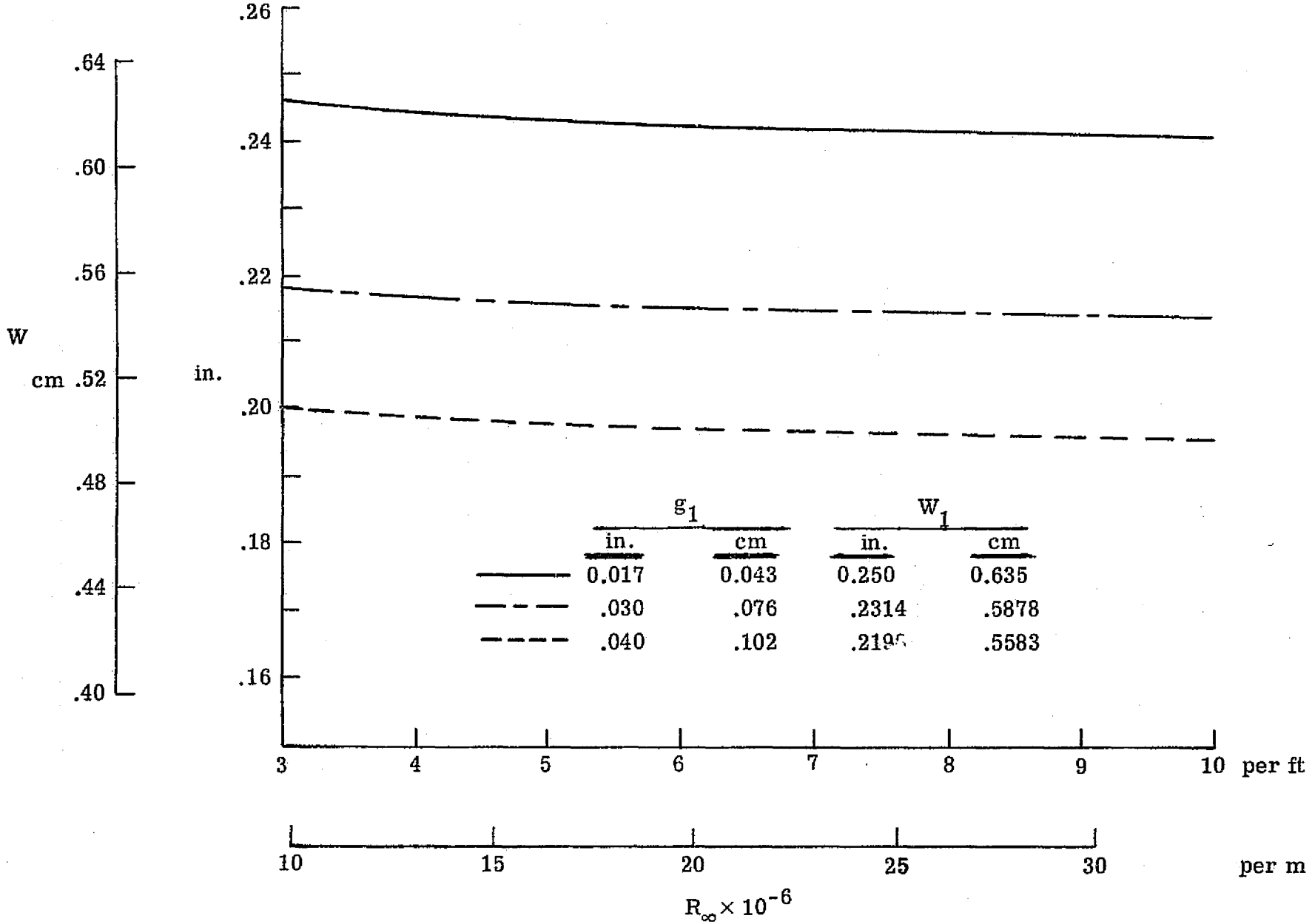

(b) Variation of W at x = 12.8 in. (32.5 cm).

Figure 5.- Concluded.

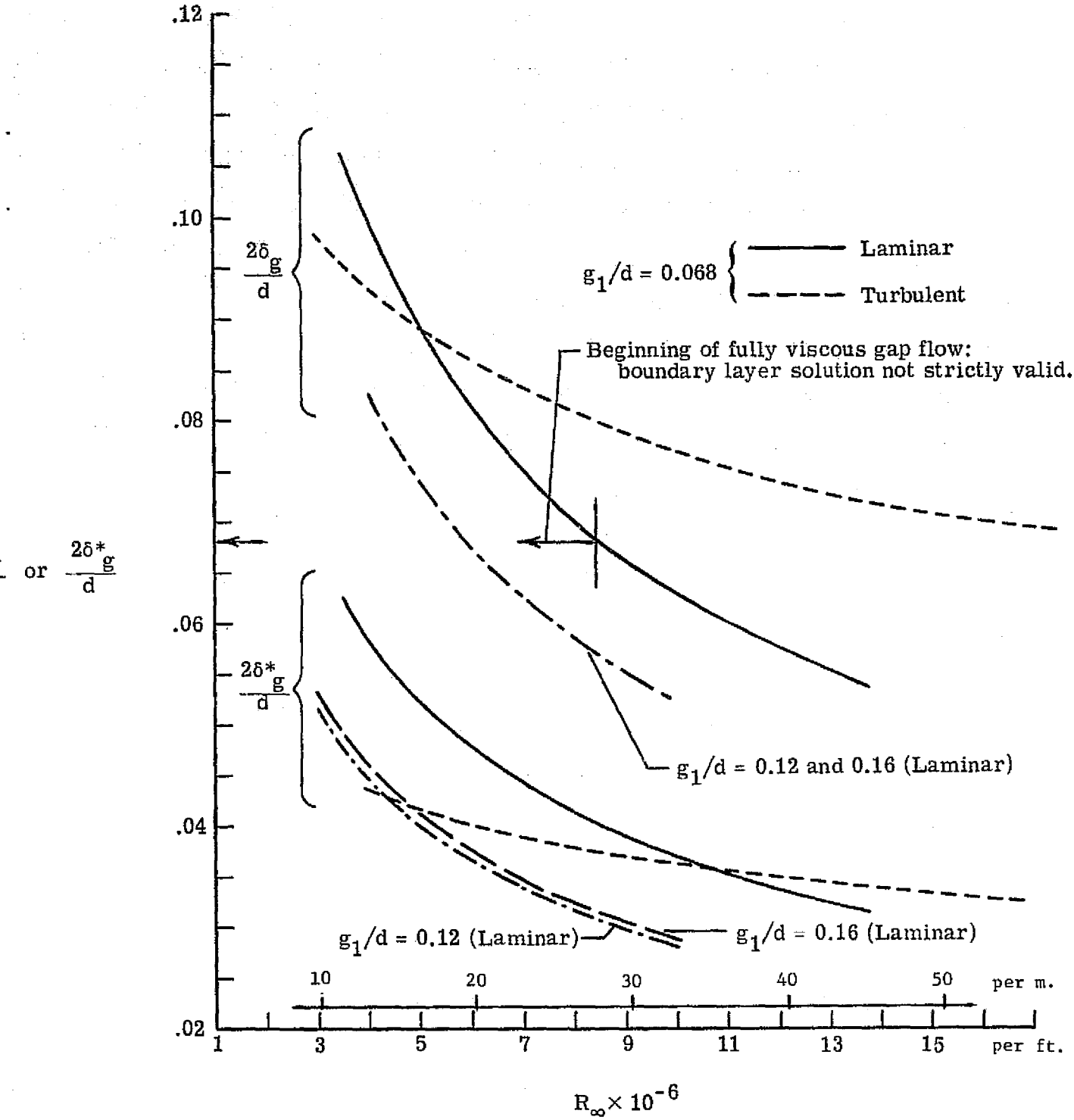

Figure 6.- Variation with freestream unit Reynolds number of boundary layer thickness and displacement thickness at the minimum slot width and at x = 0. d = 0.25 in. (0.635 cm), N = 50, r = 2 in. (5.08 cm).

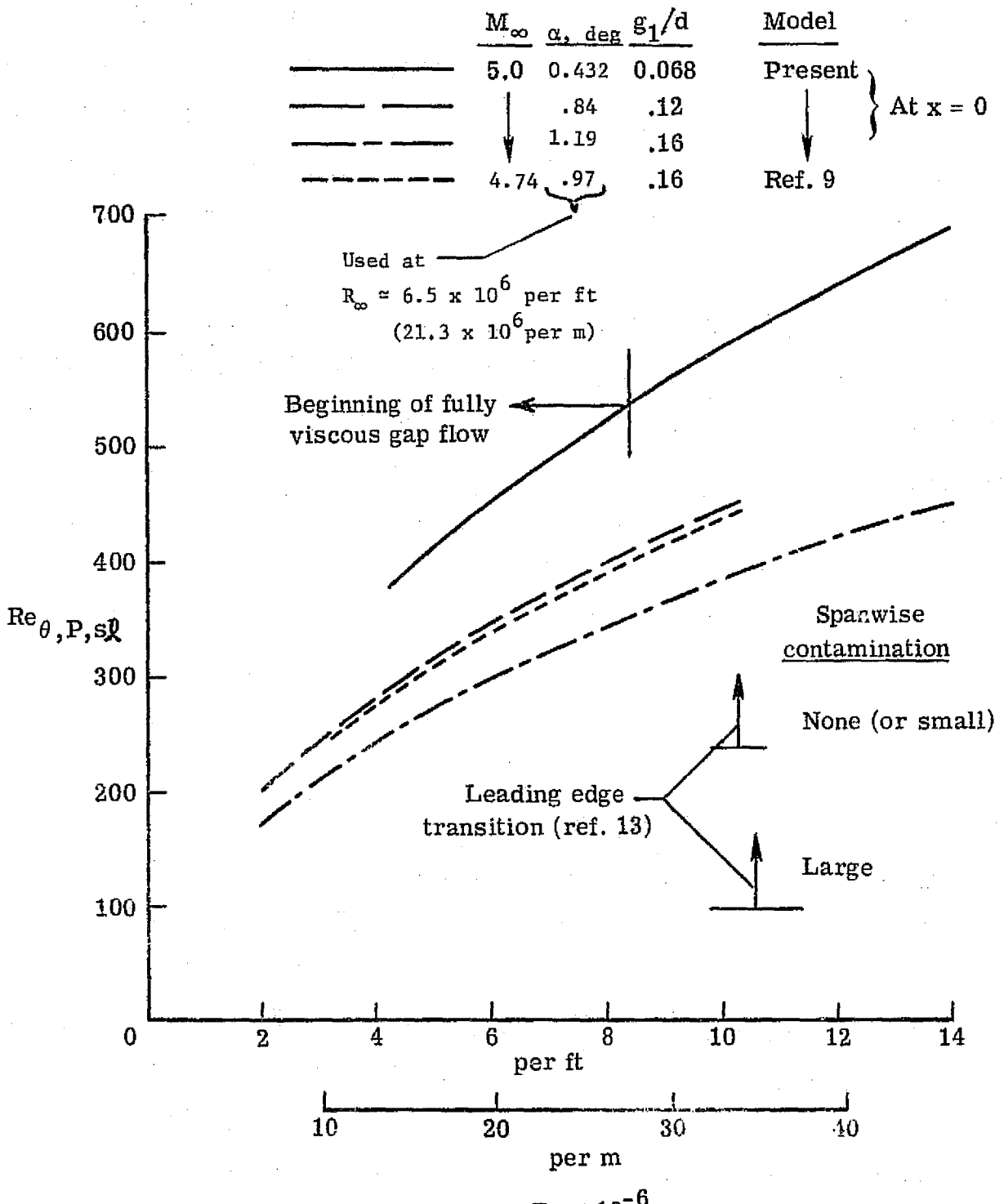

(a) Variation of Re_θ with R_∞.

Figure 7.- Effect of gap spacing on laminar boundary layer momentum thickness at the stagnation line and on the inviscid velocity distribution around rods; d = 0.25 in. (0.635 cm).

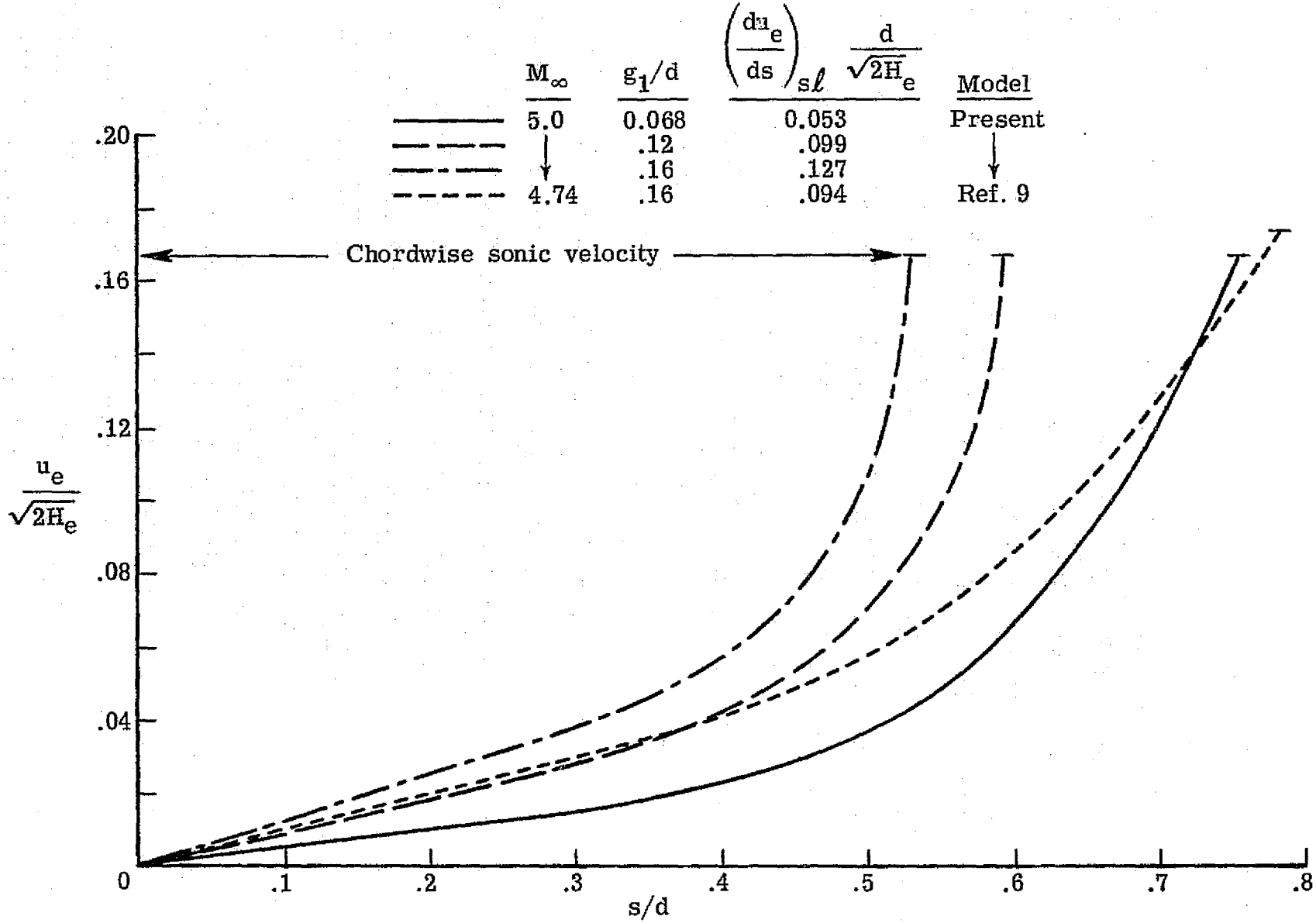

(b) Computed velocity distribution around rods.

Figure 7.- Concluded.

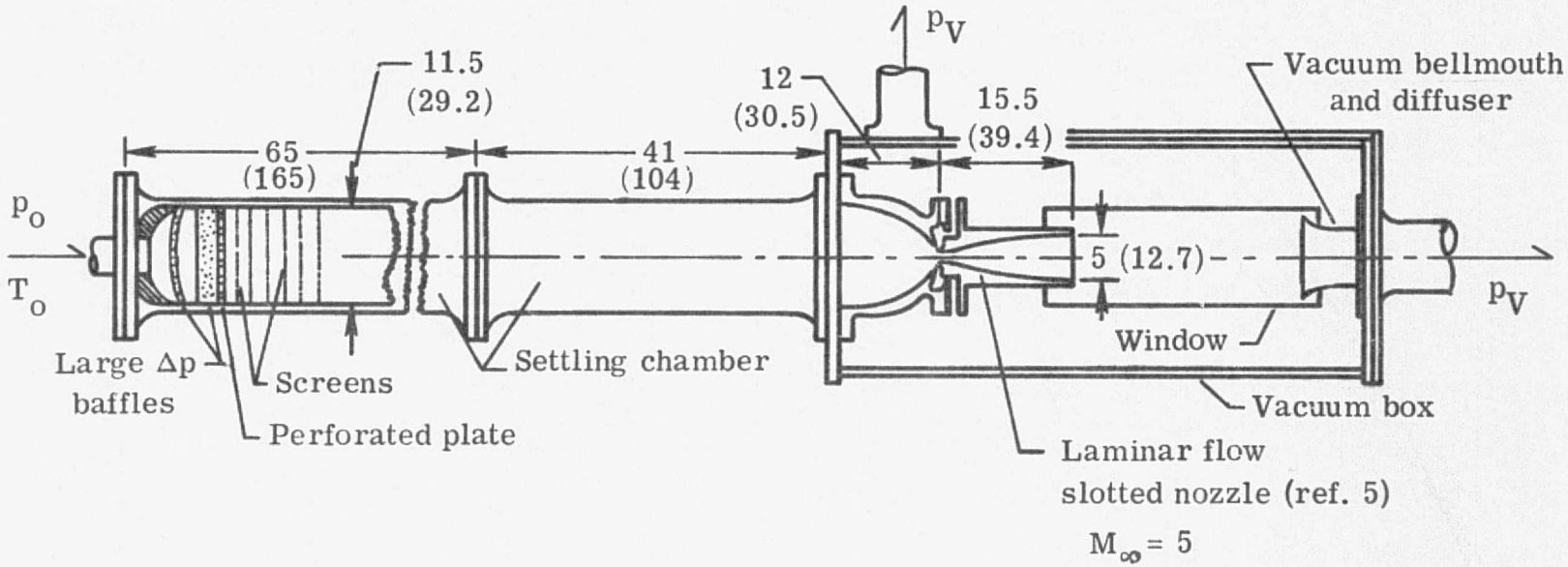

Figure 8.- Mach 5 pilot quiet tunnel. All dimensions in inches (cm).

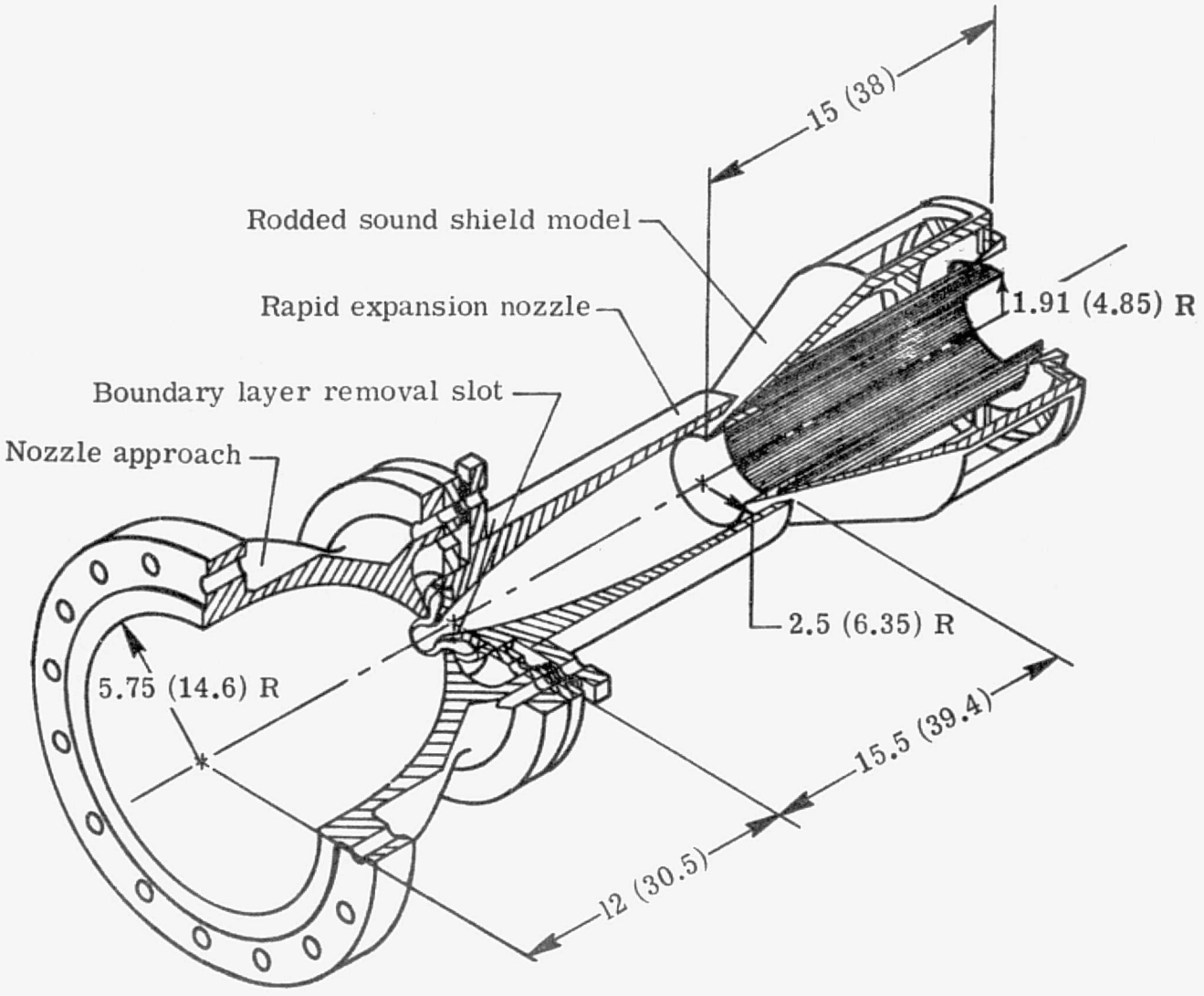

Figure 9.- Isometric sketch of rodded sound shield model mounted at exit of Mach 5 slotted nozzle. All dimensions in inches (cm).

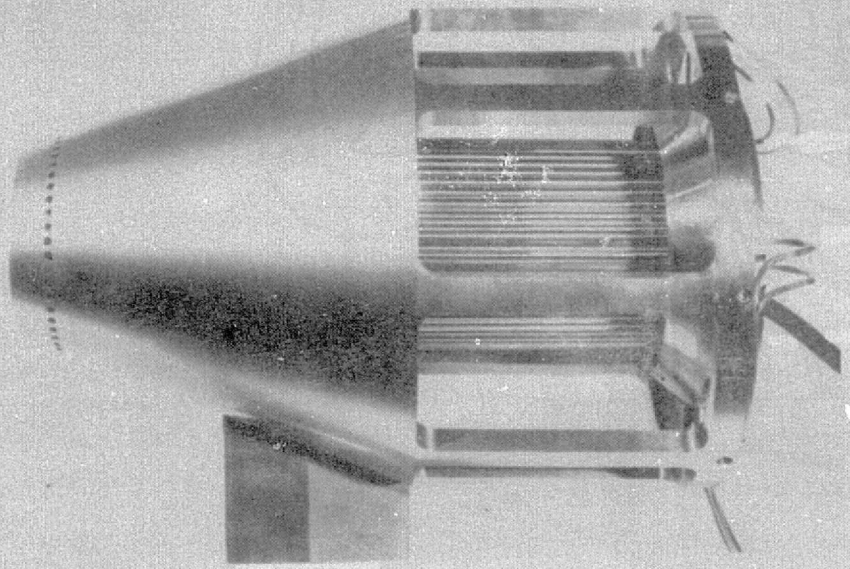

Side view

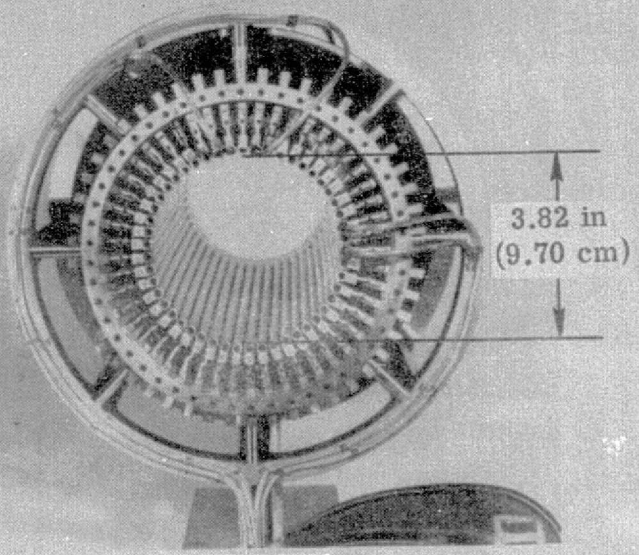

Rear view

Figure 10.- Photograph of slotted wall sound shield.

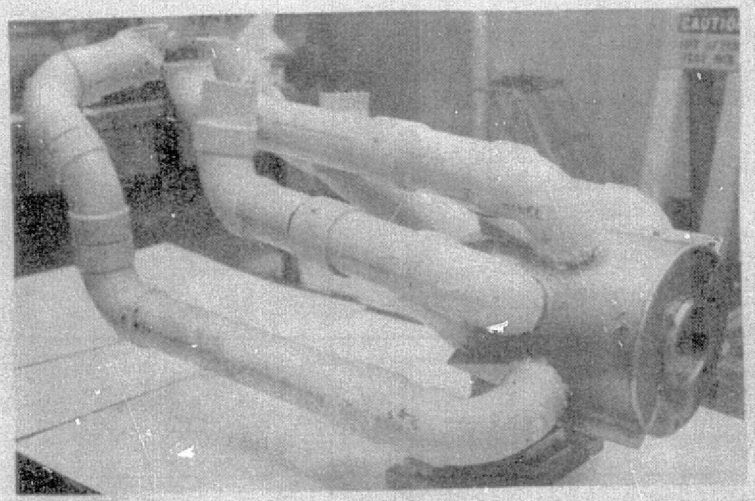

Side view

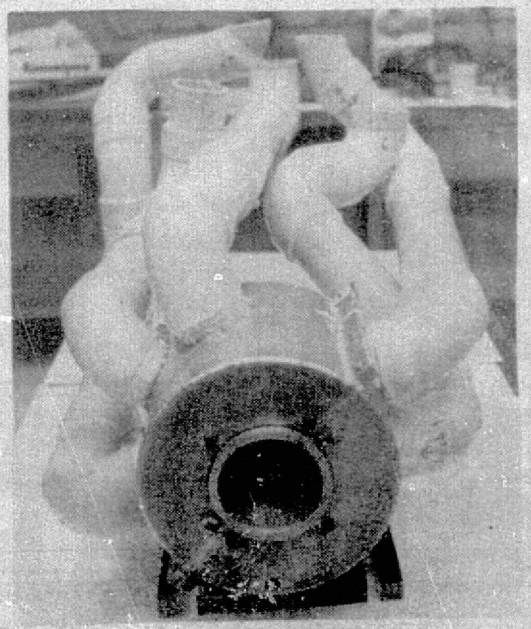

Rear view

Figure 11.- Photographs of vacuum manifold with exhaust pipes installed. Model removed from tunnel vacuum box for display.

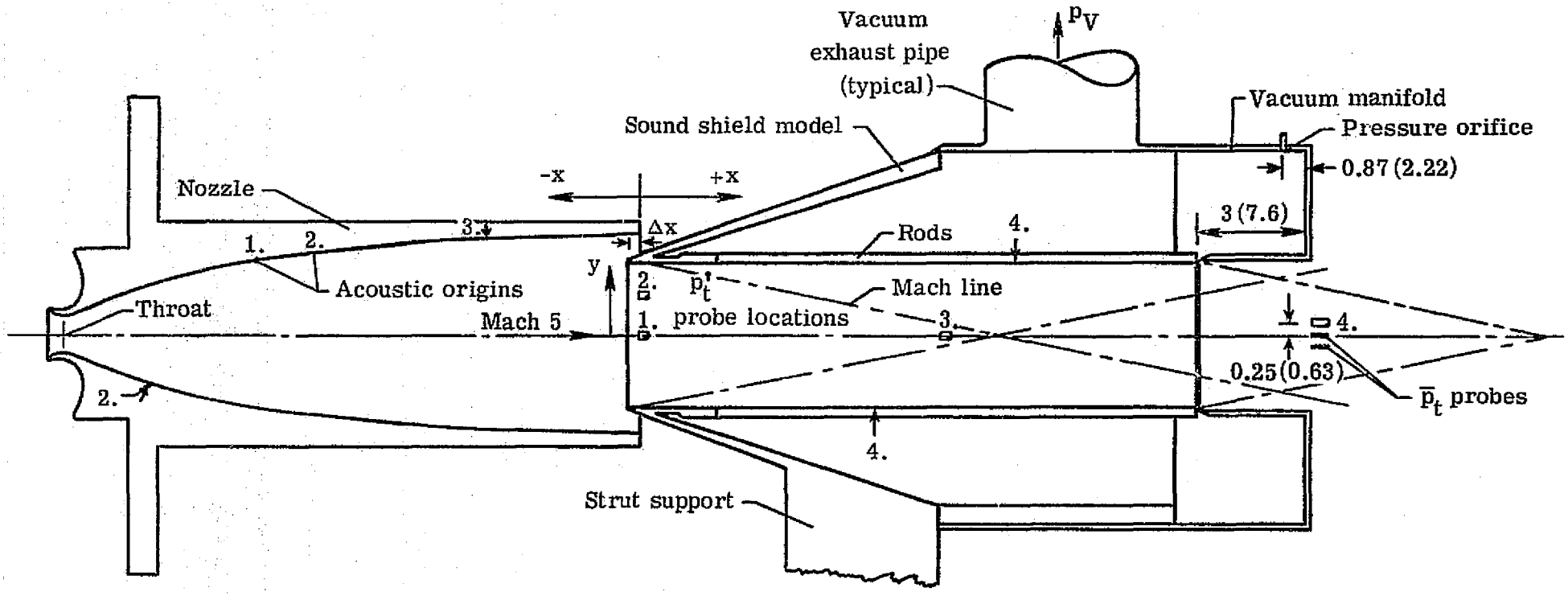

Figure 12.- Sketch of sound shield model mounted at exit of Mach 5 slotted nozzle. p_t' probe locations (1-4) and corresponding acoustic origins are shown. All dimensions in inches (cm).

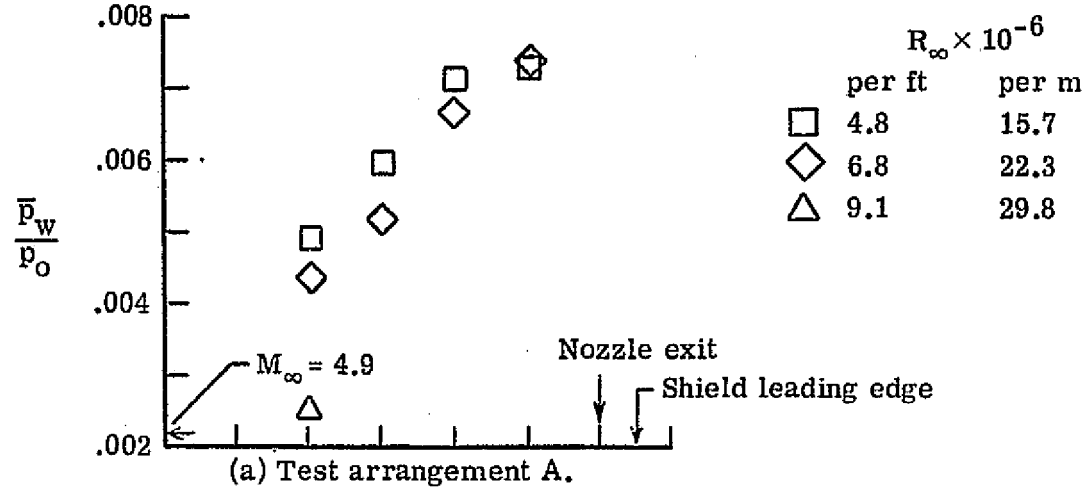

(a) Test arrangement A.

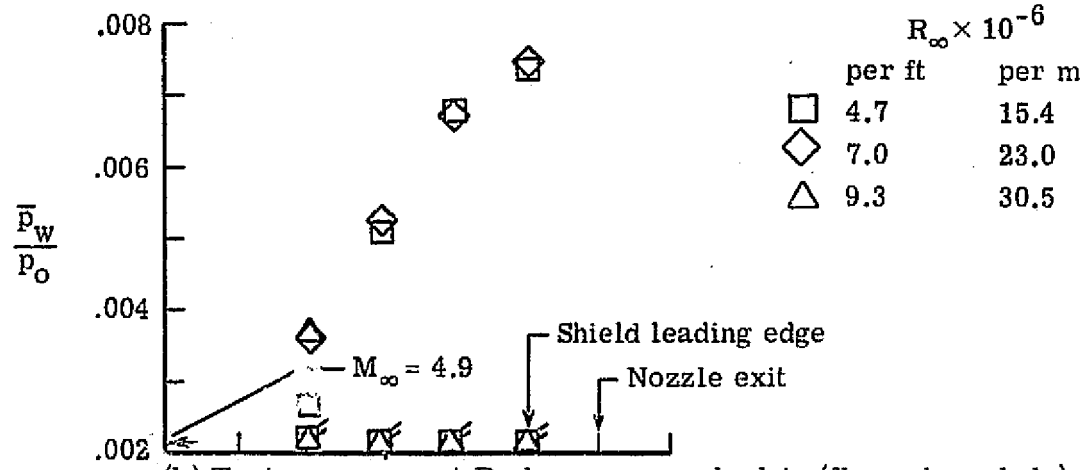

(b) Test arrangement B plus open nozzle data (flagged symbols).

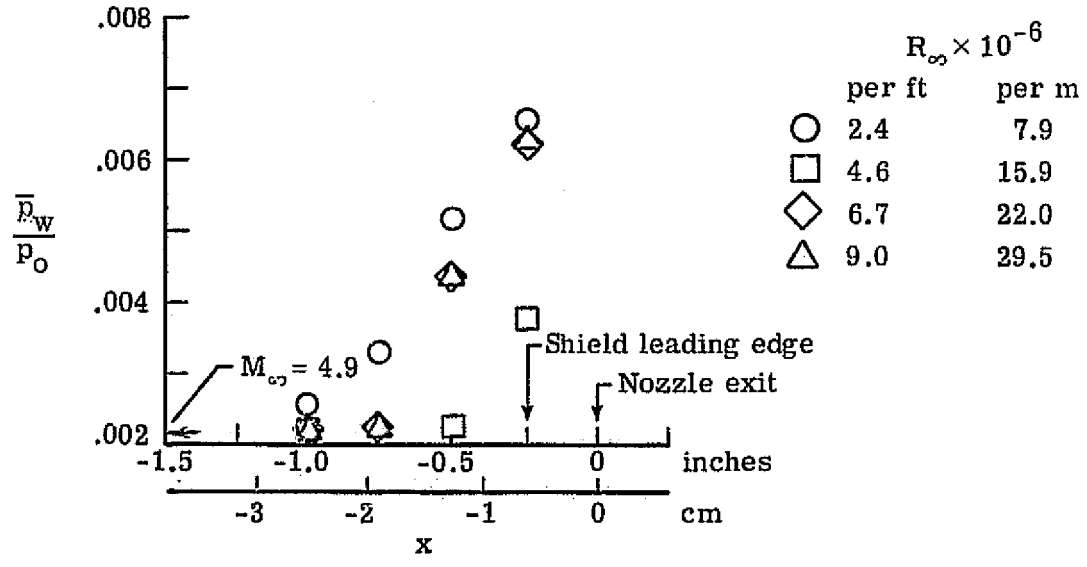

(c) Test arrangement C.

Figure 13.- Distributions of nozzle wall static pressures. Shield with $g_1/d = 0.068$, d = 0.250 in. (0.635 cm) installed near nozzle exit except as noted.

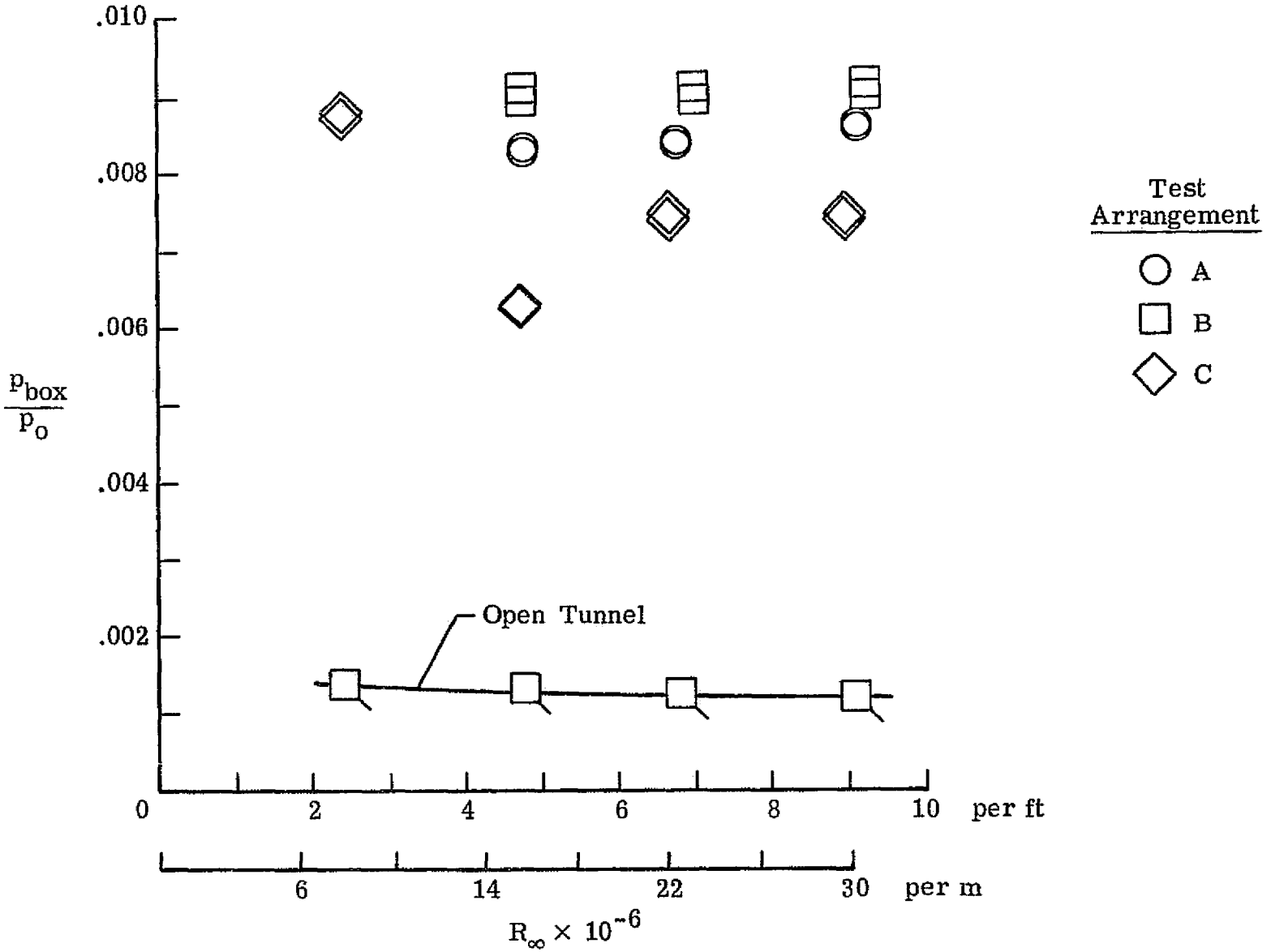

Figure 14.- Variation of tunnel vacuum box pressure with free stream unit Reynolds number. $g_1/d = 0.068$.

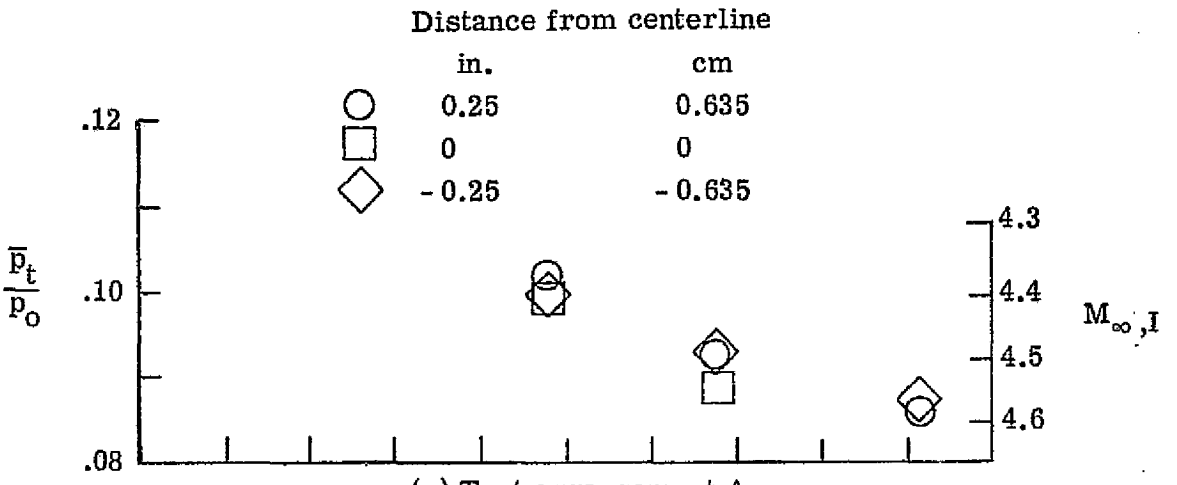

(a) Test arrangement A.

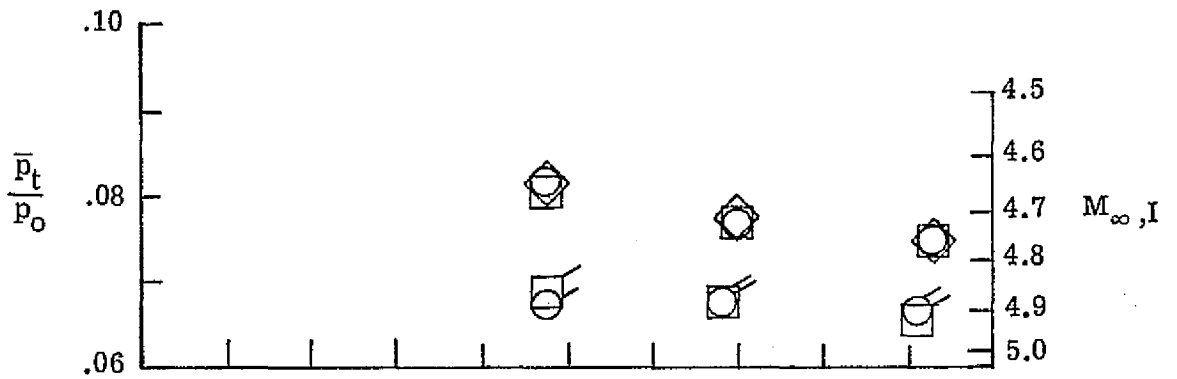

(b) Test arrangement B plus flagged symbols for open nozzle data.

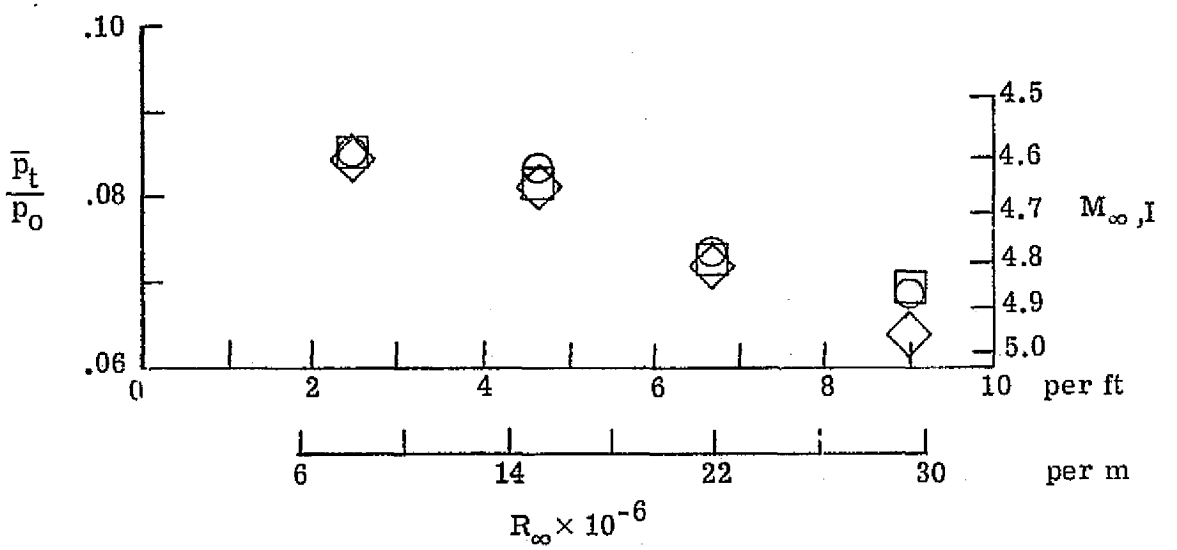

(c) Test arrangement C.

Figure 15.- Variation with freestream unit Reynolds number of mean pitot pressure at exit of vacuum manifold (see fig. 12) and at exit of nozzle. $g_1/d = 0.068$.

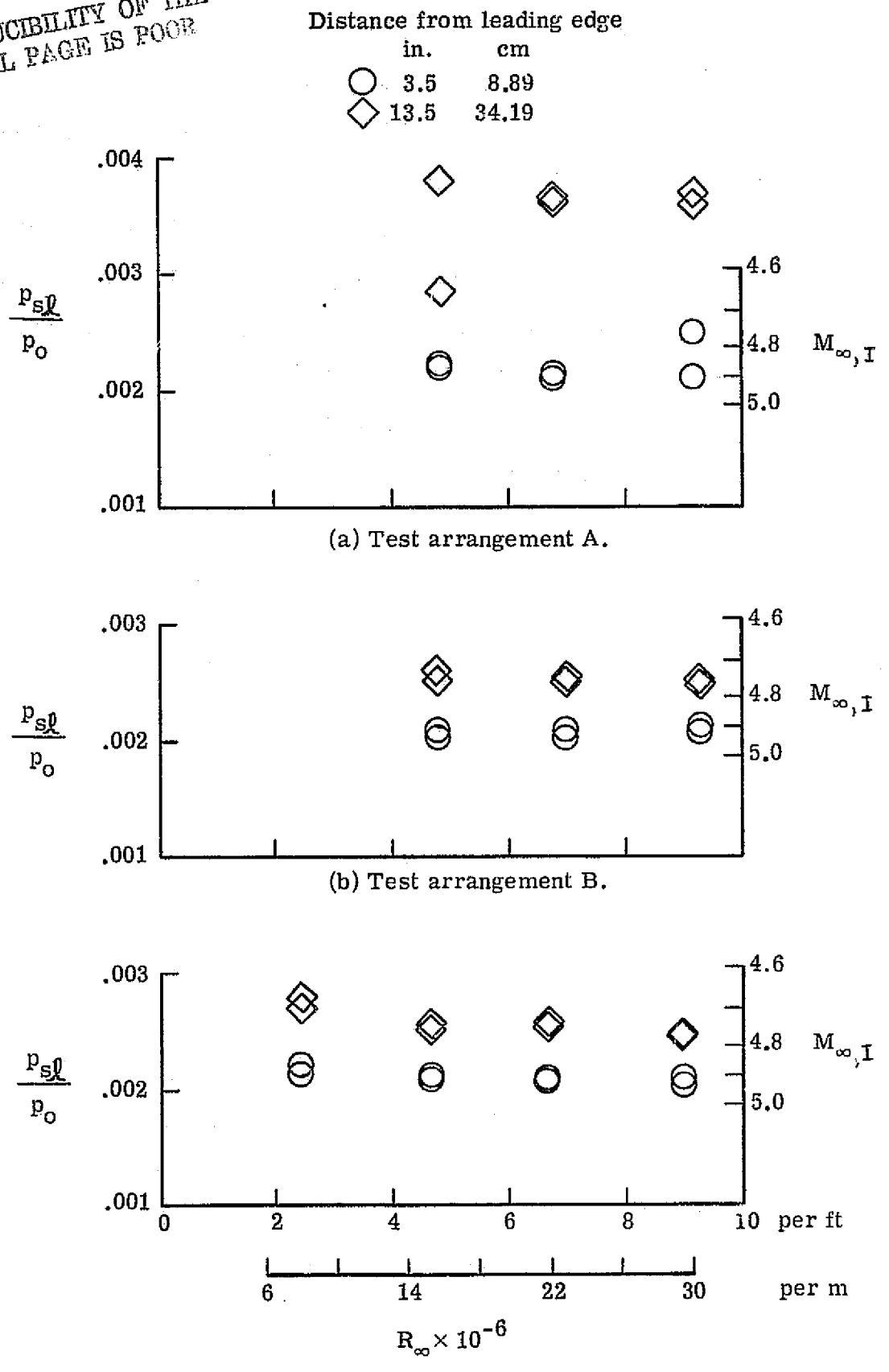

Figure 16.- Static pressures on the inside windward or stagnation line of the rods at $\phi = 0^o$.

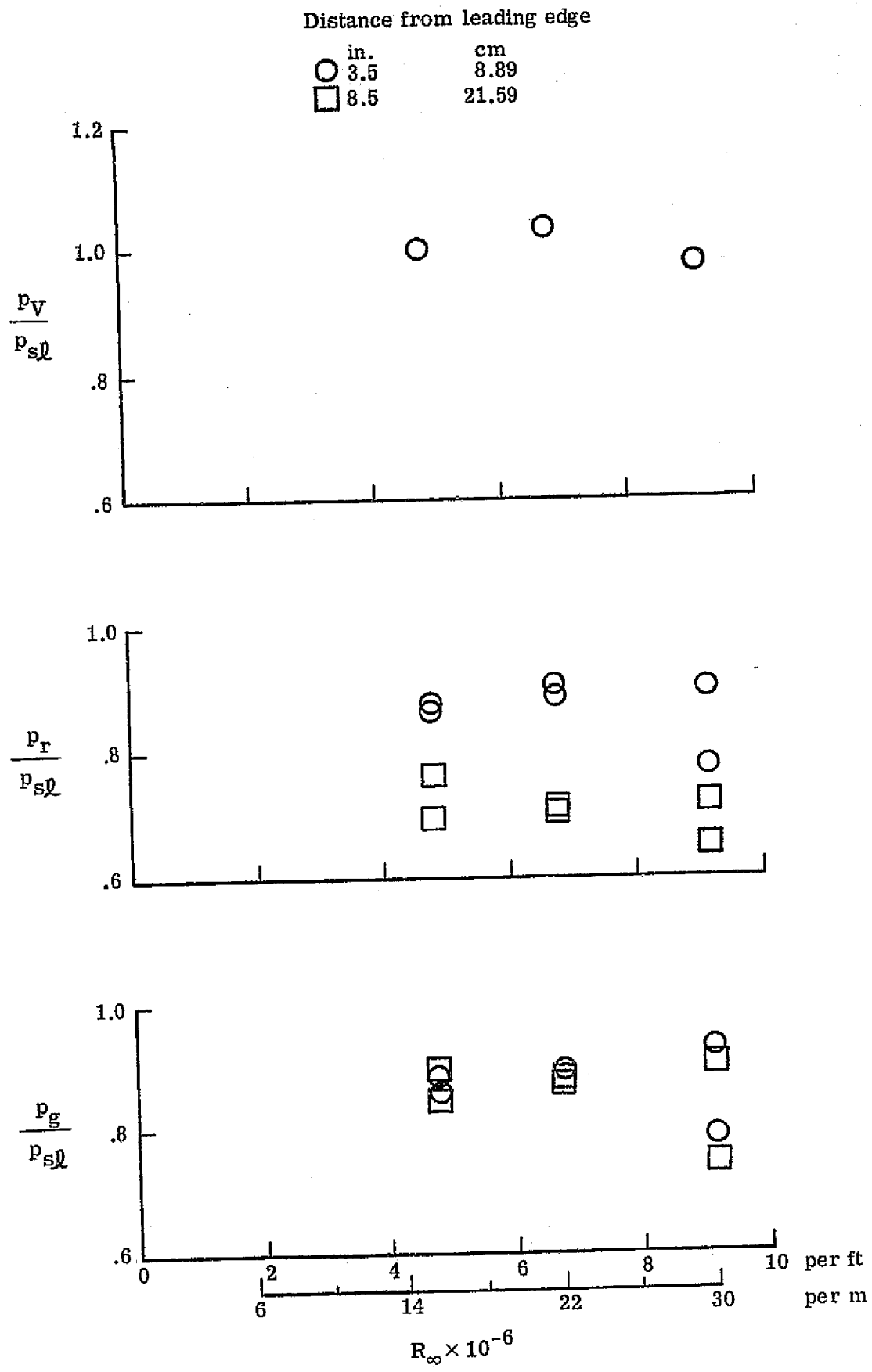

(a) Test arrangement A.

Figure 17.- Static pressures in the vacuum manifold and on the rods normalized with the rod pressures at $\phi = 0^o$. $g_1/d = 0.068$, d = 0.25 in. (0.635 cm).

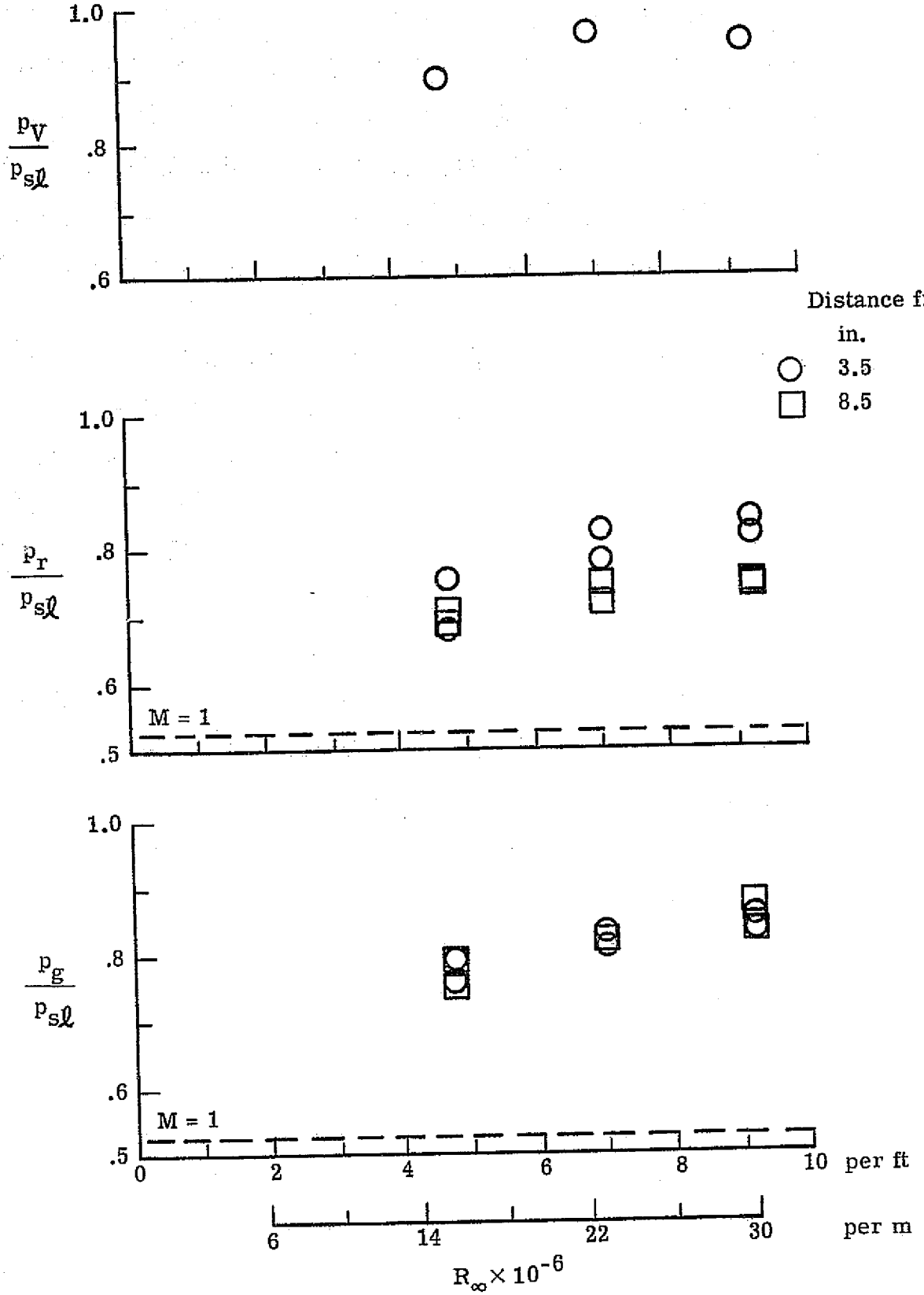

(b) Test arrangement B.

Figure 17.- Continued.

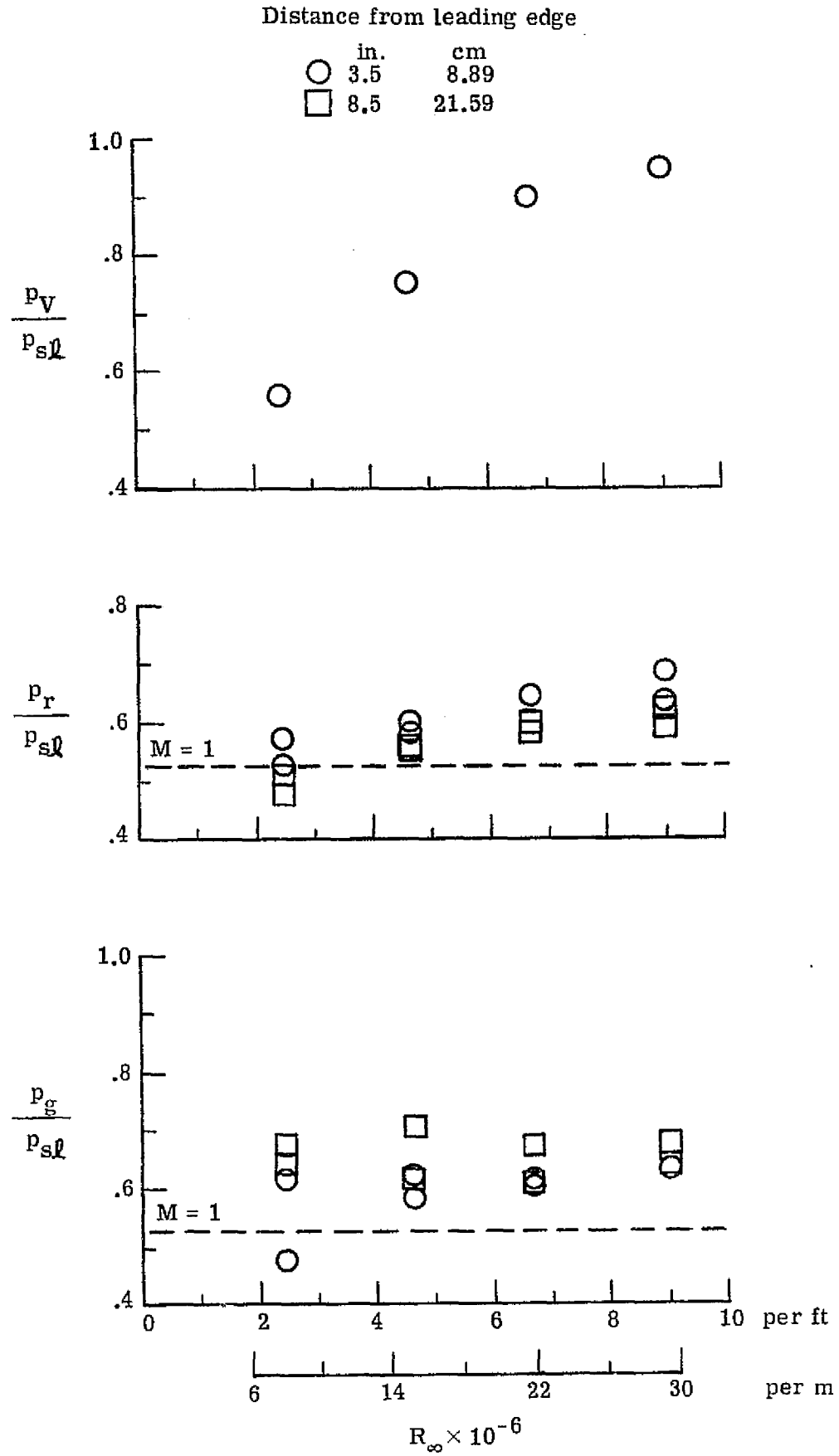

(c) Test arrangement C.

Figure 17.- Concluded.

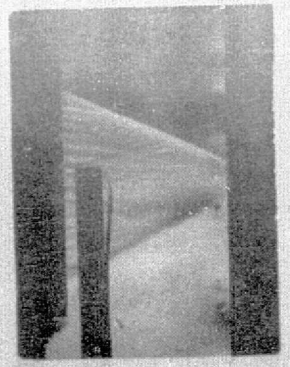

(a)

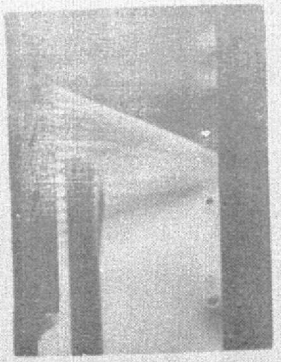

(b)

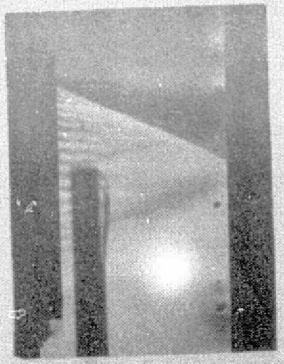

(c)

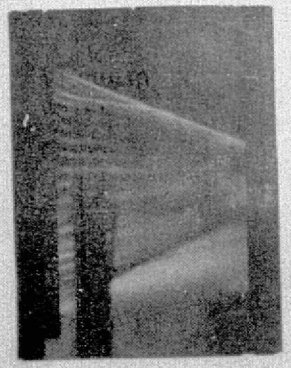

(d)

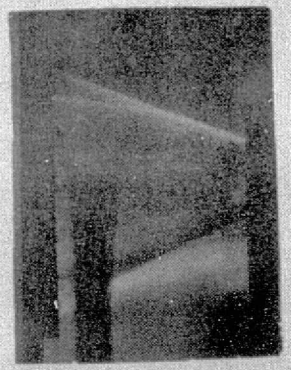

(e)

	$R_\infty \times 10^{-6}$ per ft	$R_\infty \times 10^{-6}$ per m	Test arrang.	Vacuum valve
(a)	4.8	15.7	B	Open
(b)	7.0	23.0	↓	↓
(c)	9.2	30.2	↓	↓
(d)	6.7	22.0	C	↓
(e)	6.7	22.0	↓	Closed

Figure 18.- Schlieren photographs of flow at exit of vacuum manifold. Effect of test arrangement (see table pg. 21) and vacuum for typical test conditions.

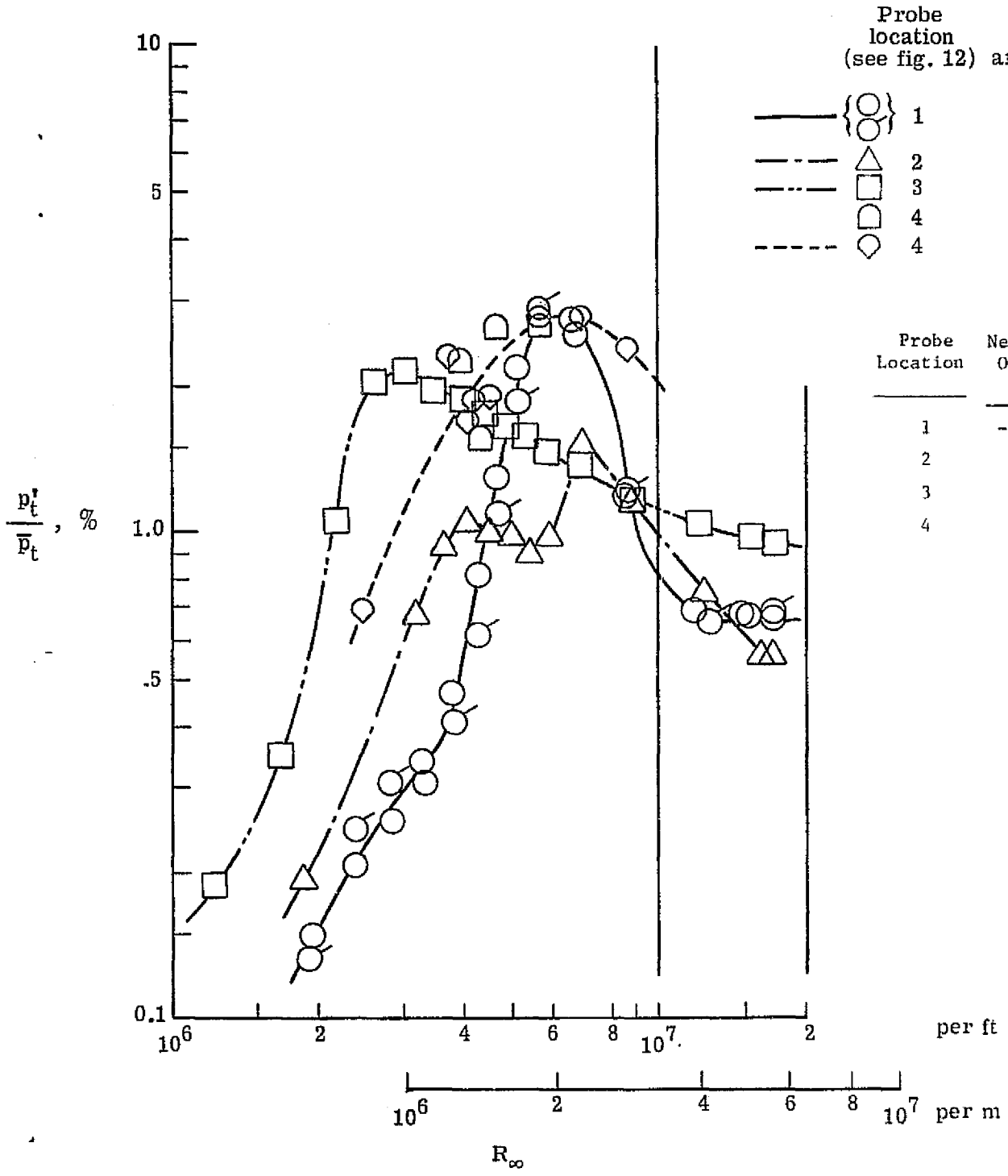

(a) $p_t'/\bar{p}_t$ variation with R_∞ for all probe locations.

Figure 19.- RMS fluctuating pitot pressures in freestream of nozzle and sound shield. See figure 12 for probe locations.

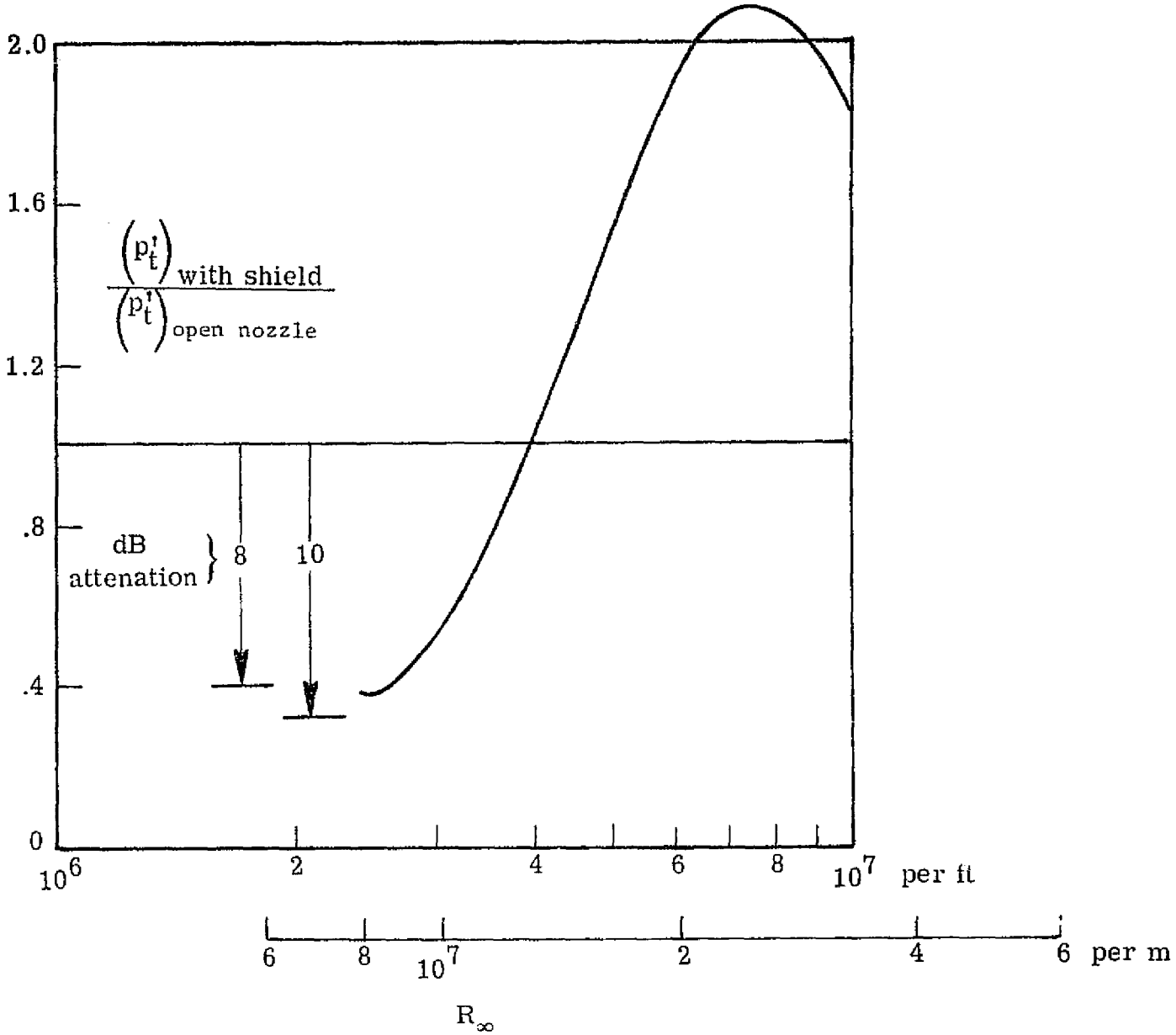

(b) Ratio of p_t' with shield to that without shield based on faired curves for probe locations 4 and 3, respectively, from fig. 19(a).

Figure 19.- Concluded.